J. Fluid Mech. (2009), *vol.* 626, *pp.* 67–109.
doi:10.1017/S0022112008005636 Printed in the United Kingdom

On the effect of heat release in turbulence spectra of non-premixed reacting shear layers

R. KNAUS† AND C. PANTANO

Department of Mechanical Science and Engineering, University of Illinois at Urbana-Champaign, 1206 W. Green St, Urbana, IL 61801, USA

(Received 28 March 2008 and in revised form 11 December 2008)

Velocity, mixture fraction and temperature spectra obtained from five direct numerical simulations of non-reacting and reacting shear layers, using the infinitely fast chemistry approximation, are analysed. Two different global chemical reactions corresponding to methane and hydrogen combustion with air, respectively, are considered. The effect of heat release, i.e. density variation, on the inertial and dissipation turbulence subrange of the spectra is investigated. Analysis of the database supports the experimentally available measurements of spectra in turbulent reacting flows showing that heat release effects can be scaled out by utilizing Favre-averaged (density-weighted) large-scale turbulence quantities. This is supported by the simulation results for velocity and mixture fraction in our moderate-Reynolds-number flows but it appears to be less supported in the dissipation subrange of the temperature spectra. The departure from universal scaling using Favre-averaged quantities in the temperature spectrum, which is evident in the dissipation subrange, appears to be caused by the strong nonlinearity of the state relationship relating the mixture fraction to the temperature, as has been suggested previously. These effects are less pronounced at intermediate wavenumbers. Analysis suggests that the nonlinear state relationship and the spectra of mixture fraction moments can be used to reconstruct the temperature spectrum across the flow. Moreover, the governing equation for the temperature variance is analysed to identify a possible surrogate for the overall rate of dissipation of temperature fluctuations and their corresponding dissipation length scale. This scaling analysis is then used to separate planes across the shear layer where the temperature dissipation length scale is alike that of the mixture fraction from regions where smaller length scales are present, and are evidenced in the dissipation subrange using Kolmogorov scaling. In our simulations, these regions correspond to the centre of the shear layer and the mean flame location. The new estimate for the temperature dissipation length scale is able to collapse the compensated spectra profiles at all planes across the shear layer for all simulations.

1. Introduction

The turbulence scales in reacting flows differ from those in non-reacting flows by the presence of density (and temperature) variations throughout the flow that not only alter momentum exchanges but also modify the transport coefficients of the fluid. The difference between the enthalpies of formation of the reactants and products leads to heat release which increases the temperature and decreases the density. The ratio

† Email address for correspondence: rknaus2@illinois.edu

between the temperature of the cold reactant streams and that of the hot products is roughly 4–6 for hydrocarbon combustion in gas turbine combustors and roughly 7 for room temperature reactant streams. As is well known, heat release induces changes on the dynamics of the large scales of the turbulence, possibly coupling with buoyancy effects if the Richardson number, the ratio of potential energy to kinetic energy, of the flame is sufficiently large. This is relatively well understood from available quantitative measurements of instantaneous and averaged velocity profiles in a good number of canonical and practical flows. Nevertheless, less is known regarding the behaviour of the small scales of turbulence in the presence of heat release. Apart from a fundamental interest in the problem, the small scales are important because combustion in most practical regimes takes place always at finite rates within these small scales. When the spatial and temporal scales of the chemical conversion become comparable to those of the turbulence, e.g. in flames, there is 'turbulence–combustion interaction', that is, strong coupling between turbulent fluctuations and the reaction progress occurs. Turbulent combustion modelling that attempts to eliminate the details of the internal structure of the flames is challenging and it requires a deeper understanding of the dynamics and spatial structure of the interaction. This affects modelling in large-eddy simulation (LES), where the low-wavenumber turbulence spectrum is accurately simulated but the small scales are modelled, and in transported probability density function (p.d.f.) approaches, where closure for the molecular transport terms is required (Pope 1985). In this paper, we discuss only results pertaining to heat release effects in the non-premixed mode of combustion, where reactants are initially segregated and mixing is a fundamental requirement of the chemical conversion. We utilize the flame-sheet approximation, which assumes that the chemical reaction occurs on a time scale much shorter than the smallest relevant time scale of the flow and essentially imposes a one-way coupling between chemistry and turbulence accounting solely for heat release effects. This helps isolate phenomena that are purely caused by the heat released in the flow and eliminates the complex, but important, flame structure changes and dynamics present in real flames close to the extinction/reignition regime, which are not considered here.

Theoretical analyses of the structure of the reaction zone in stationary conditions range from the infinitely-fast-chemistry limit of Burke & Schumann (1928) (see also Williams 1985) to the more accurate models describing details of the internal structure of the flame using large-activation-energy asymptotics for one-step kinetics (Liñán 1974) and multi-step kinetics (Seshadri & Peters 1988). In turbulent flames, understanding the chaotic dynamics of the velocity and the complex system of chemical reactions is a challenging problem (Peters 1984; Bilger 1988). Theoretical studies identify the rate of dissipation of mixture fraction fluctuations, referred to as the 'scalar dissipation' for simplicity, as an important quantity relating mixing to chemistry. The role of other quantities – including the strain rate field, chemistry details, detailed transport properties and unstationarity – remains an open issue. The scalar dissipation is defined as $\chi = 2D\nabla Z \cdot \nabla Z$, where D is a suitable average diffusion coefficient. We follow the customary approach to define χ based on Z instead of its fluctuation, an approximation that is good for high-Reynolds-number flows. In reacting flows D can vary substantially in different regions of the flow owing to its dependence on temperature. Experimental investigations of the behaviour of the statistics of χ include, for example, Namazian, Schefer & Kelly (1988); Gladnick, LaRue & Samuelsen (1990); Boyer & Queiroz (1991); Nandula, Brown & Pitz (1994); Everest *et al.* (1995); Chen & Mansour (1996); Buch & Dahm (1998); Fielding, Schaffer & Long (1998); Karpetis & Barlow (2002); Tsurikov & Clemens (2002); Su

& Clemens (2003); Barlow & Karpetis (2004); Noda *et al.* (2005); Wang, Clemens & Varghese (2005); and Markides & Mastorakos (2006). Complementary numerical studies, primarily using direct numerical simulations (DNS), have also verified some of the experimental findings, e.g. Vedula, Yeung & Fox (2001); Schumacher, Sreenivasan & Yeung (2005); and Donzis, Sreenivasan & Yeung (2005). Reviews by Warhaft (2000), Bilger (2004), Sreenivasan (2004), and Dimotakis (2005) discuss many of the known features associated with χ, primarily for non-reacting flows.

Experimental diagnostic advances are now capable of simultaneous measurements of species and temperature in non-premixed turbulent flows and they have provided a dramatic improvement of our understanding of the chemical conversion process and the internal structure of real turbulent flames. It is known from previous studies that reaction takes place on thin surface-like flames even for jets at high Reynolds numbers (e.g. Dibble, Masri & Bilger 1987; Seitzman *et al.* 1990; Everest *et al.* 1995; Masri, Dibble & Barlow 1996; Donbar, Driscoll & Carter 1999; Meier *et al.* 2000). It has been shown that heat release diminishes the rate of growth of turbulent shear flows when compared with equivalent non-reacting flows (Wallace 1981; McMurtry *et al.* 1986; Hermanson & Dimotakis 1989; Muñiz & Mungal 2001; Theron & Bellenoue 2006; Mahle *et al.* 2007). Modelling concepts have been developed to relate the effect of heat release, or density variation, on these flows (Tacina & Dahm 2000; Dahm 2005). Moreover, numerous experimental and computational studies have elucidated that the structural behaviour – specifically the composition and the flow around non-premixed flames – is substantially different from that observed in non-reacting flows (Donbar, Driscoll & Carter 1998; Vervisch & Poinsot 1998; Han & Mungal 2000, 2003). These changes are more prominent at the smallest scales of the flow for non-premixed combustion since the process is mixing limited. For large flow-to-chemical time scale ratio (Damköhler number) the flame thickness is small with respect to the Kolmogorov scale and the effect on the flow is essentially equivalent to a finite heat release deposition around the stoichiometric surface. The temperature and density gradients around the peak heat release zone are very small because the profiles exhibit a peak there. Recent progress allowing measurement of both composition and flow velocity at the reaction zone (Carter, Donbar & Driscoll 1998; Rehm & Clemens 1998; Han & Mungal 2003) is providing a more comprehensive picture of the details of the turbulence–combustion interaction in these flows. This paper provides complementary results on the behaviour of turbulence spectra in reacting flows where the level of heat release is large, typical of hydrocarbon/hydrogen combustion. The effects of heat release on the inertial and dissipation subranges of the velocity, mixture fraction and temperature spectra are investigated. While it is expected that many (if not most) aspects of these spectra should resemble that of non-reacting flows, some details emerge to be different primarily owing to the heat release effect, e.g. changes of the statistics of χ with heat release have already been investigated (Pantano, Sarkar & Williams 2003). The implications and importance of spectra in modelling of reacting flows is discussed further by Sabini, Shieh & Givi (1996).

Statistical arguments applied to the turbulence energy cascade (Richardson 1922) by Kolmogorov (1941*a*,*b*) assume that, for sufficiently high Reynolds numbers, the statistics of the small scales of motion have a universal form uniquely determined by the turbulence rate of dissipation, $\tilde{\epsilon}$, and the kinematic viscosity, $\tilde{\nu}$. Additionally, the statistics of the scales of motion between the integral and dissipative scales have a universal form determined uniquely by $\tilde{\epsilon}$, independent of $\tilde{\nu}$ (e.g. Tennekes & Lumley 1972; Pope 2000). Tildes are used to denote density weighted averages to maintain a uniform notation throughout the text with $\tilde{\epsilon}$ and $\tilde{\nu}$ reverting to their incompressible

values for constant density flows. The large scales, low-wavenumber range of the energy spectrum, are widely recognized to depend on the problem geometry and as such they are not relevant to the present discussion. In this paper we are concerned with the study of the effect of heat release on the scalings proposed by Kolmogorov's theory in the inertial and in the dissipation subrange of the turbulence spectra of reacting flows. It is common to model turbulent reacting flows by neglecting the effect of heat release on the behaviour of the small turbulence scales. This assumption builds on results by Kolmogorov (1961) who extended his previous theory by considering the turbulence dissipation as a spatially varying quantity with a certain (intermittent) statistical distribution to support the mounting experimental evidence that $\tilde{\epsilon}$ is not constant throughout the flow (Batchelor & Townsend 1949). It is then shown that the turbulence spectrum is only weakly affected by the non-uniformity of $\tilde{\epsilon}$ (Monin & Yaglom 1971). Therefore, one could extend this theoretical framework to reacting flows and assume that the changes in viscosity by heat release could be factored out as part of the statistical variations of $\tilde{\epsilon}$. This argument appears plausible in the inertial subrange but it is less convincing in the dissipation subrange, where variations of $\tilde{\nu}$ induced by heat release may need to be taken into account.

Theoretical results have so far concentrated on the spectra of active scalars but with negligible heat release (Corrsin 1961; Bilger 1980; Bilger, Saetran & Krishnamoorthy 1991; Kosály 1993). A more detailed numerical investigation of the behaviour of the spectra of reactive scalars has been reported by de Bruyn Kops, Riley & Kosály (2001), where the effect of varying Damköhler number is investigated. Experimental measurements of spectra of reactive flows remain scarce in contrast to non-reacting flows (e.g. Uberoi & Freymuth 1969; Wygnanski & Fielder 1969; Birch *et al.* 1978; Dowling & Dimotakis 1990; Antonia & Mi 1993). Furthermore, in those cases where some data is available, it is often limited to a few quantities (Kounalakis, Sivathanu & Faeth 1991; Renfro *et al.* 2000) usually not including the velocity field, except for Zhang, Wang & Tong (2004) who reported velocity-scalar increment p.d.f.. The experimental measurements by Wang *et al.* (2005) and Nagel & Dahm (2007) have been used to investigate the effects of variable density on the turbulence spectra. Their results suggest that after appropriate scaling the effect of heat release on the inertial turbulence scales is remarkably small. Moreover, given that this part of the spectrum is energetically dominant (contains most of the temperature variance), deviations owing to heat release in the dissipation subrange should only account for a small amount of the overall spectral transfer, that is, the total variance of the mixture fraction is relatively insensitive to deviations in the dissipation subrange compared to either energy-containing or inertial subrange. From a different point of view, previous results by Everest *et al.* (1995) suggest that mixing effects may explain differences in chemical composition in some stages of jet flames, while Wang, Karpetis & Barlow (2007) argue that there is sufficient spectral separation between the temperature fluctuations affecting $\tilde{\nu}$ and the strain rate to prevent a strong interaction in the dissipation subrange. Kaiser & Frank (2007) and Frank & Kaiser (2008) report measurements of the temperature dissipation spectrum including cutoff length scales for a turbulent reacting jet. Frank & Kaiser (2008) finds that non-reacting estimates for the cutoff length scale are comparable on the centreline but were significantly less accurate off-centreline. Experiments by Wang & Barlow (2008) measured the dissipation cutoff length scale of the temperature field and found it to be equal to or lower than the corresponding length scale for the mixture fraction. Additionally, experiments by Wang *et al.* (2008) observed enhanced high-wavenumber content for the temperature spectrum. They argue that this results from the temperature state

relationship $T^e(Z)$. The argument is that the temperature exhibits a local peak each time the mixture fraction crosses the stoichiometric mixture fraction, which in turn causes the temperature field to exhibit smaller scale structures than the mixture fraction. At locations far away from stoichiometry, the state relation is nearly linear and thus the cutoff scale of the temperature spectrum is nearly that of the mixture fraction. The present study provides further simulation-derived evidence supporting a reduction of the dissipation length scale of the temperature owing to heat release and a collapse of the velocity and mixture fraction spectra using Favre-averaged scaling.

2. Flow description

The flow considered in this study is a temporally evolving reacting shear layer between fuel and oxidizer streams. This flow was simulated using DNS for different fuels and at different levels of heat release. The numerical formulation of the compressible Navier–Stokes equations with the infinitely-fast-chemistry approximation is used. High-order spatial and temporal discretization is employed to solve the governing equations; further details can be found in Pantano *et al.* (2003). The coordinate directions are denoted as $\boldsymbol{x} = (x_1, x_2, x_3) = (x, y, z)$, corresponding to the streamwise, transverse and spanwise directions, respectively. Periodic boundary conditions are imposed in the x_1 and x_3 directions.

2.1. *Simulation parameters*

Three flow conditions are analysed in this study: a non-reacting case (labelled simulation A), three methane–air cases with global reaction $CH_4 + 2O_2 \rightarrow CO_2 + 2H_2O$ (referred to as simulations B, C and C′) and a hydrogen–air case with global reaction $H_2 + \frac{1}{2}O_2 \rightarrow H_2O$ (labelled simulation D). The viscosity μ was assumed constant except for case C′ that assumed $\mu(T) \sim T^{0.7}$. The oxidizer stream in each simulation consists of a mixture of oxygen and nitrogen with a mass fraction of oxygen equal to 0.23 to approximate air. The fuel stream consists of a mixture of methane (simulations B, C and C′) or hydrogen (simulation D) diluted with nitrogen. The corresponding fuel mass fractions are 0.23 for methane and 0.06666 for hydrogen with stoichiometric mixture fraction of $Z_s = 0.2$ and 0.3, respectively. These values correspond to an equivalence ratio, $\phi = (1 - Z_s)/Z_s$, of 4 and 2.3333, respectively. The reactant streams were diluted with air in order to allow convenient resolution of temperature gradients on the fuel side of the shear layer. In this case, the dilution moves the flame closer to the centre of the shear layer where there would be greater interaction between the turbulence and the heat release. Studies by Clemens & Paul (1995) and Pickett & Chandhi (2003), among others, show that the reaction zone still stands to one side of the mixing layer even at these relatively high stoichiometric mixture fraction values, a behaviour that is similar to that of combustion of pure hydrocarbons with air (having a lower Z_s).

Additionally, the temperature of the oxidizer stream in the methane–air simulations was raised by roughly 20 % in order to achieve constant density of both free streams. In the case of the hydrogen–air simulation, the temperature of both free streams was equal, leading to a fuel stream with substantially lower density. Simulations B and C are documented in more detail in Pantano *et al.* (2003) (also denoted there as simulations B and C). The same formulation and computer code was used to perform the new simulations A and D.

Thermochemical parameters of the ideal-gas mixture were non-dimensionalized using a reference temperature of $T_o = 298$ K and the specific heat coefficient of

Species	C_p^0	C_p^1	W	$\Delta h^0/C_{pO_o}T_o$
H_2	15.9201	0.4737	2	0
CH_4	2.4655	0.8743	16	−17.149
O_2	1.0000	0.0639	32	0
H_2O	2.0110	0.2187	18	−49.814
CO_2	0.9347	0.1321	44	−33.168
N_2	1.1397	0.0553	28	0

TABLE 1. Thermochemical parameters normalized by the reference temperature $T_o = 298$ K and the reference specific heat of oxygen at this temperature $C_{pO_o} = 905$ J kg^{-1}K^{-1}.

oxygen, C_{pO_2}, at T_o. The specific heat coefficients of species were given a linear dependence on temperature, $C_{pi} = C_{pi}^0 + C_{pi}^1(T-1)$, valid over the temperature range of interest (300–2300 K) in accordance with thermochemical data (Lide 1999), where T denotes the non-dimensional temperature. The standard enthalpy of formation is denoted by Δh_i^0 and molecular weight is W_i for species i (see table 1). Finally, the heat release parameter is defined by

$$Q = \frac{q_o Y_{F,f} Z_s}{C_{pN_o} T_o \nu_F W_F}, \tag{2.1}$$

where subscript F denotes fuel properties, with $Y_{F,f}$ denoting the mass fraction of fuel in the fuel stream and ν_F denoting the stoichiometric coefficient of the fuel in the global reaction. The enthalpy of the reaction is defined as

$$q_o = \sum \nu_i W_i \Delta h_i^o. \tag{2.2}$$

The adiabatic flame temperature T_f is obtained from the isobaric energy conservation equation and varies with Q and the chemistry details (Williams 1985).

Simplified transport properties were used in the simulations to focus attention on a few key phenomena. Accordingly, the viscosity μ is taken to be constant in all cases but C′. The independence of the viscosity on the temperature makes 'relaminarization' of the flow less important at the Reynolds numbers considered here. There is nonetheless a reduction in Reynolds number corresponding to decreases in density near the flame in cases B, C and D. In the hydrogen–air case especially, there would be significant changes in the dynamic viscosity owing to the heat release which are neglected in this approximation. The scalar diffusion coefficient D was chosen such that the Schmidt number $Sc = \mu/\rho D$ was constant and equal to 1.0 in case A and 0.7 in the remaining simulations. The thermal conductivity κ was chosen such that the Prandtl number $Pr = \mu C_p/\kappa$ was also constant and equal to 0.7, the approximate value for air, resulting in a constant Lewis number $Le = Sc/Pr = 1.0$ in all the reacting simulations. The species mass fractions Y_i were assumed to have identical diffusion coefficients, which in the infinitely-fast-chemistry limit allows Y_i to be related uniquely to the mixture fraction (Burke & Schumann 1928). This choice also eliminates the effects of differential diffusion in the simulations which is expected to be small in regard to the effect of heat release on the flow dynamics for fast methane–air and hydrogen–air combustion. The initial Reynolds number is defined as $Re = \rho_o \Delta u \delta_{\omega,o}/\mu$, where ρ_o denotes the average of the free-stream densities, Δu is the velocity difference between the two streams and the initial vorticity thickness, defined below, is denoted as $\delta_{\omega,o}$. The convective Mach number of all the simulations based on the free-stream

Case	A (air)	B (methane–air)	C–C′ (methane–air)	D (hydrogen–air)
Q	–	3.73	7.46	7.90
T_f	–	4.20	6.82	6.73
N_x	768	768	768	2048
N_y	258	258	258	512
N_z	192	192	192	512
$L_x/\delta_{\omega,o}$	31	31	31	92
$L_y/\delta_{\omega,o}$	20	20	20	29
$L_z/\delta_{\omega,o}$	8	8	8	23

TABLE 2. Initial parameters of the simulations.

conditions was set to 0.3 to minimize any effect owing to compressibility. Further initial parameters of the simulations are reported in table 2.

The simulations were initialized with a hyperbolic-tangent profile for the velocity and mixture fraction that matched the fixed free-stream parameters defining the conditions of the simulations, from where all other derived quantities can be inferred. Incompressible velocity fluctuations with a model isotropic turbulence spectrum are added to the laminar initial conditions to help the flow transition to turbulence as quickly as possible. The shear layer thickness grows approximately linearly with time and the simulations are stopped when domain size effects become apparent. This is visible in two-point correlations of the streamwise velocity which cease to be completely decorrelated for large separations. Further details can be found in Pantano *et al.* (2003).

2.2. *Statistics*

The statistics of the shear layer are obtained as density-weighted (Favre) averages, defined for a field $\psi(\boldsymbol{x})$ as

$$\tilde{\psi} = \frac{\overline{\rho\psi}}{\overline{\rho}}, \tag{2.3}$$

where the overline indicates ensemble (Reynolds) average. All statistics, $\tilde{\psi}$ or $\bar{\psi}$, depend on x_2 for the shear layer flow considered here. Additionally, every field can be decomposed into a mean and fluctuating component denoted by $\psi' = \psi - \overline{\psi}$ and $\psi'' = \psi - \tilde{\psi}$ for Reynolds and Favre fluctuations, respectively. Favre-based averages are used throughout the presentation when scaling quantities are required, unless stated otherwise. This ensures that all non-dimensional terms revert naturally to their incompressible counterparts when the density of the flow is constant and uniform.

The Reynolds number based on the vorticity thickness is defined as

$$Re_{\omega,cold} = \frac{\rho_o \Delta u \delta_\omega}{\mu_o}, \qquad Re_{\omega,hot} = \frac{\Delta u \delta_\omega}{\nu_h}, \tag{2.4}$$

where ρ_o and μ_o denote the average of the cold free-stream densities and viscosity, respectively, and ν_h denotes the maximum planar average kinematic viscosity. The vorticity thickness δ_ω is defined according to

$$\delta_\omega = \frac{\Delta u}{\left|S_u\right|_{max}}, \tag{2.5}$$

with

$$S_u = \frac{\partial \tilde{u}_1}{\partial x_2}, \qquad S_Z = \frac{\partial \tilde{Z}}{\partial x_2}, \qquad S_T = \frac{\partial \tilde{T}}{\partial x_2}, \tag{2.6}$$

denoting the streamwise velocity, mixture fraction and temperature gradients, respectively.

The turbulence kinetic energy is defined by

$$\tilde{k} = \frac{\widetilde{u''_m u''_m}}{2}, \tag{2.7}$$

and the turbulence dissipation is defined by

$$\tilde{\epsilon} = \frac{1}{\bar{\rho}} \overline{\left(\boldsymbol{\sigma}'_{ik} \frac{\partial u'_i}{\partial x_k} \right)}, \tag{2.8}$$

where $\boldsymbol{\sigma}_{ik}$ is the Newtonian stress tensor. The scalar dissipation is defined by

$$\tilde{\chi} = \frac{2}{\bar{\rho}} \overline{\left(\rho D \frac{\partial Z'}{\partial x_k} \frac{\partial Z'}{\partial x_k} \right)}. \tag{2.9}$$

Using these quantities, the Kolmogorov scale is defined as

$$\tilde{\eta} = \left(\frac{\tilde{\nu}^3}{\tilde{\epsilon}} \right)^{1/4}, \tag{2.10}$$

where $\tilde{\nu} = \overline{\mu/\rho}$. The Taylor-scale Reynolds number is determined through the isotropic relationship

$$\tilde{\epsilon} = 15\tilde{\nu} \frac{u'^2}{\lambda^2} = 5\tilde{\nu} \frac{q}{\lambda^2}, \tag{2.11}$$

where q is the turbulence intensity defined by $q = \sqrt{2\tilde{k}/3}$. This gives the Taylor-scale Reynolds number,

$$Re_\lambda = \frac{q\lambda}{\tilde{\nu}} = 2\tilde{k} \sqrt{\frac{5}{\tilde{\nu}\tilde{\epsilon}}}. \tag{2.12}$$

Finally, the Reynolds number based on the integral scale ℓ is defined according to

$$Re_\ell = \frac{q\ell}{\tilde{\nu}} = \frac{3}{20} Re_\lambda^2, \tag{2.13}$$

where ℓ is the integral scale (e.g. Pope 2000). All results reported in this paper are obtained at the end of these simulations, before domain size effects become visible in two-point statistics. Therefore, no further references to time will be made below since all analysed quantities are concerned with the spatial structure of the turbulent flow at a fixed time. Some key final simulation parameters are shown in table 3. These denote the resolution, final Kolmogorov-to-grid size ratio and peak integral and Taylor microscale Reynolds number.

Figure 1 shows average profiles of streamwise velocity, mixture fraction, density and temperature for all simulations at the last instant of time, where spectra will be analysed in the following sections. The average streamwise velocity profile $\tilde{u}_1$ has a hyperbolic-tangent-like profile that is qualitatively similar in all simulations and is also similar between the average mixture fraction profiles. The specific value of Z_s in the reacting cases induces an asymmetry in the average velocity and mixture fraction profiles, with the value of $\tilde{u}_1 = 0$ and $\tilde{Z} = 0.5$ occurring slightly closer to the oxidizer stream. The average density profile has a minimum towards the oxidizer side of the

Case	A	B	C	C′	D
$Re_{\omega,cold}$	6057	12, 600	10, 400	68, 743	24, 138
$Re_{\omega,hot}$	6057	4447	2446	3890	5264
$Re_{\ell,peak}$	1915	1622	1008	1685	1782
$Re_{\lambda,peak}$	113	104	82	106	109
$\eta_{min}/\Delta x$	0.45	0.36	0.46	0.23	0.61
$(x_2/\delta_\omega)_s$	–	0.3335	0.3406	0.3516	0.1687

TABLE 3. Derived parameters of the simulations at the end of the runtime. The subscript 'peak' denotes the maximum planar average value of the quantity in the shear layer. The last row denotes the location of the mean stoichiometric surface $\tilde{Z}((x_2/\delta_\omega)_s) = Z_s$.

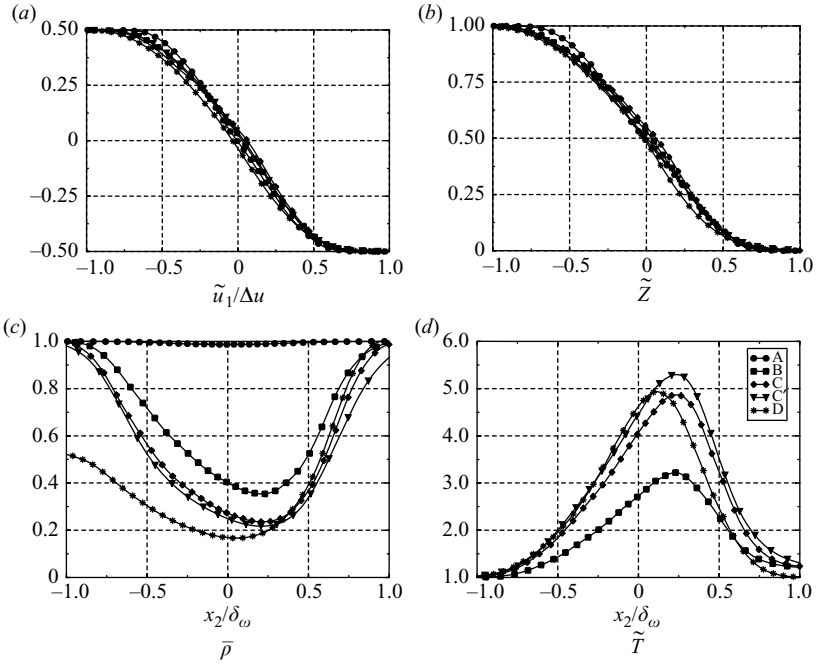

FIGURE 1. Average profiles of velocity (*a*), mixture fraction (*b*), density (*c*) and temperature (*d*) for all simulations.

shear layer where the flame tends to be located in average. The temperature of the oxidizer stream in the methane–air simulations was set to achieve equal density in the fuel and oxidizer free streams. This was not done for the hydrogen case. The profile in the hydrogen case shows a significant density difference between the oxidizer and fuel streams. In all cases, the density reaches a minimum near the mean stoichiometric mixture fraction plane, although slightly shifted towards the fuel side. The temperature profile in each case has a peak on the oxidizer side of the shear layer with a magnitude that is controlled by the stoichiometry of the mixture.

Figure 2 shows mixture fraction, density and temperature variances as well as turbulence kinetic energy for all simulations. The variance of the mixture fraction peaks at the centre of the shear layer, where the turbulence kinetic energy also peaks, and decreases as one moves away from the centre of the shear layer. The density and temperature variance profiles have two peaks on each side of the centre of the shear

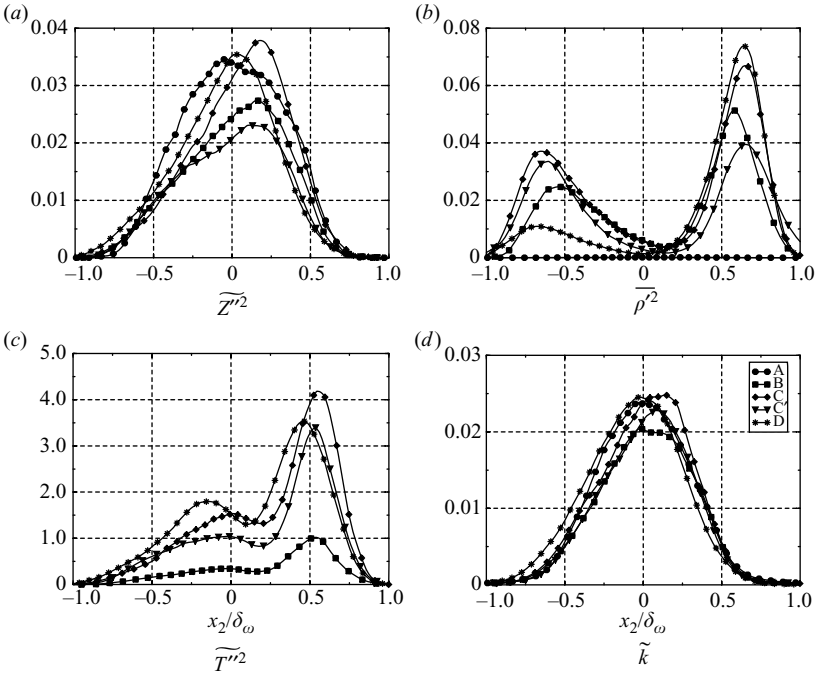

FIGURE 2. Mixture fraction (*a*), density (*b*) and temperature (*c*) variances and turbulence kinetic energy (*d*) profiles for all simulations.

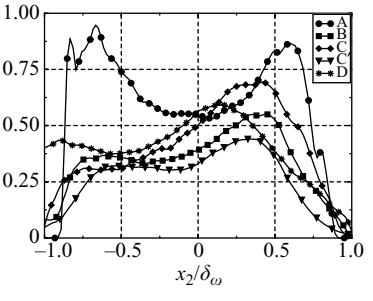

FIGURE 3. Level of unmixedness across the shear layer for all simulations.

layer with the profiles decreasing towards the free streams. These two different peaks are caused by the asymmetric temperature gradients in the shear layer induced by the stoichiometry of the mixture. Figure 3 shows the level of unmixedness, usually defined as

$$I(x_2/\delta_\omega) = \frac{\widetilde{Z''^2}}{\tilde{Z}(1-\tilde{Z})},$$

across the shear layer for all simulations. This index is zero when the flow is perfectly mixed, $\widetilde{Z''^2} = 0$, and one when the flow is completely unmixed. In the simulations, I is below 0.55 at the centre of the shear layer for all cases, indicating that substantial mixing is taking place. Finally, figure 4 shows the turbulence and scalar dissipation for all simulations. It is shown that all profiles peak towards the centre of the shear

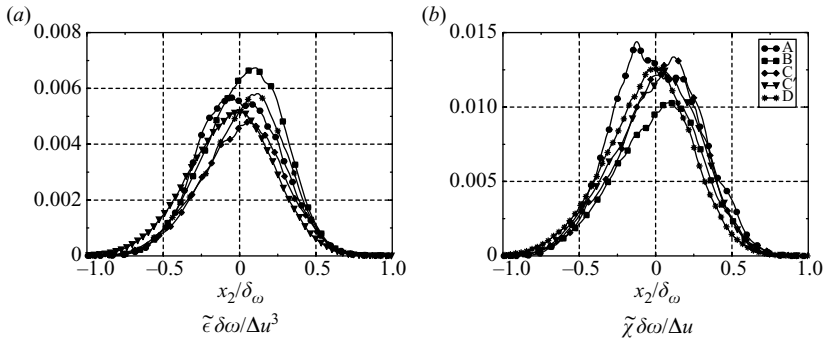

FIGURE 4. Normalized turbulence (*a*) and scalar (*b*) dissipation profiles for all simulations.

layer. There is a slight shift of the scalar dissipation peak towards the location of the average stoichiometric mixture fraction value, which is more pronounced for case B.

3. Spectra

The one-dimensional spectra of velocity, mixture fraction and temperature as well as the cospectra between velocity and mixture fraction and velocity and temperature were extracted from the simulations for analysis. While the two-dimensional spectrum is of general interest, in practice only the one-dimensional (line) spectrum has been investigated exhaustively experimentally. We refer to the line autospectrum as the spectrum for simplicity throughout the paper from this point onwards, unless stated otherwise. Results at different planes across the shear layer (various x_2) are reported in order to study the behaviour of the spectrum at different representative locations. The following planes were investigated for the reacting cases: P_0 corresponding to the plane of peak mixture fraction variance (generally very close to the centre of the shear layer) and marked in the figures with circles, P_1 corresponding to the plane of the lower peak of density variance and marked with diamonds, P_2 corresponding to the plane of the higher peak of density variance and marked with triangles and P_s denoting the plane where the Favre-averaged mixture fraction $\tilde{Z}(x_2)$ equals the stoichiometric mixture fraction value Z_s, which are marked by squares. The planes P_1, P_2 and P_s are not defined in the non-reacting simulation A. Therefore, in this case, P_0 was defined as the centre of the shear layer for the non-reacting case (making comparisons with the reacting simulations straightforward) while P_1 and P_2 denote the locations where $\tilde{Z}(x_2)$ takes the values of the stoichiometric mixture fraction in the methane and hydrogen case, denoted by left and right triangles, respectively. Finally, it was observed that normalization of the wavenumber with $\tilde{\eta}$ and the spectra with $\tilde{\epsilon}$ and $\tilde{\chi}$ helped collapse the spectra of all simulations in the inertial and sometimes in the dissipation subrange (at all investigated planes across the shear layer). For this reason, it was deemed appropriate to use this scaling in all figures appearing in the next sections. Note that it is not claimed here that the Favre averages are the only, or the most appropriate, averaging technique one could use to scale all spectra under all circumstances. It is only observed that using the standard Favre-averaged quantities for the turbulence and mixture fraction dissipation was sufficient to collapse the turbulence energy and mixture fraction spectra. The only ambiguity that remains is the definition of the Kolmogorov scale in (2.10) since there are several possible manners to define an average kinematic viscosity, $\tilde{\nu}$, for a variable density

flow. It was observed that using the Reynolds-averaged version $\overline{\mu/\rho}$ or the alternative Favre-averaged version $\bar{\mu}/\bar{\rho}$ produced indistinguishable results.

3.1. *Turbulence energy spectra*

The one-dimensional turbulence energy spectrum is defined by

$$E^{1D}(\kappa_1) = \frac{1}{2}\left(F_{uu}^{1D} + F_{vv}^{1D} + F_{ww}^{1D}\right), \tag{3.1}$$

where each term on the right-hand side denotes the power-spectrum of the u, v and w velocity components, respectively, according to (3.1). Following Kolmogorov theory, the scaling of the turbulence spectra for incompressible flows approximately obeys a $-5/3$ power-law in wavenumber. This can be extended to variable density flows by assuming

$$E^{1D}(\kappa_1) = C_K \tilde{\epsilon}^{2/3} \kappa_1^{-5/3} e^{-\beta \kappa_1 \tilde{\eta}}, \tag{3.2}$$

where C_K is a proportionality constant, approximately equal to 1.6. The approximately exponential decay of the spectrum in the dissipation subrange or roll-off, as initially suggested by Kraichnan (1959), has also been included in this scaling for completeness. Figure 5 shows the one-dimensional energy spectra taken in the streamwise wavenumber direction for all simulations and planes considered in this study. It is observed that the spectra bends gradually and it appears to have a well-defined dissipation subrange in all the simulations but there is no unequivocal inertial ($-5/3$) subrange in these simulations, although the Reynolds number is moderately high. It is observed that the profiles are well collapsed using the Favre-based scaling statistics (see discussion below for plane P_1 of case C′). These results are in agreement with those reported recently by Nagel & Dahm (2007).

Further investigation of the behaviour of E^{1D} in the dissipation subrange is better accomplished by plotting the compensated spectrum, which represents $\kappa_1^{5/3} E^{1D}$ in logarithmic coordinates (figure 6) or linear-logarithmic coordinates (figure 7). The latter exposes the approximately exponential decay of the dissipation subrange. Figure 6 indicates that the inertial subrange, if present, is rather short, and generally valid conclusions about the behaviour of the inertial subrange cannot be inferred from the present data. The data appears to collapse in the intermediate range of wavenumbers but a power-law behaviour is not indisputable. Furthermore, it is observed that the agreement between the model spectra, (3.2) with $C_K = 1.6$, for case A is not as good as the comparisons with the reactive cases. The reasons for this discrepancy are not known at this point but it may be worth recalling that the non-reactive shear layer exhibits large-scale organized structures which are not seen in the reactive cases (Brown & Roshko 1974) and their presence may require a somewhat different value of the scaling factor C_K than that used in the figures. Figure 7 shows results for all cases at all planes, indicating that the exponential decay rate, (3.2), is close to the experimental value of $\beta \approx 5.2$ (Saddoughi & Veeravalli 1994). There is a rather small amount of variability in β for all the reacting cases as opposed to the non-reacting case which shows negligible variation across planes. In general, all cases exhibit a remarkable good collapse in the dissipation subrange, and the small amount of variability supports the conjecture that Kolmogorov's scaling holds for the turbulent reacting shear layer remarkably well, even at planes of the shear layer located relatively close to the free streams. The simulation results suggest that heat release does not affect the velocity spectra in a significant manner when rescaled in terms of Favre-averaged statistics. This observation does not imply that the large scales of the flow are not affected by the variations in density throughout the domain.

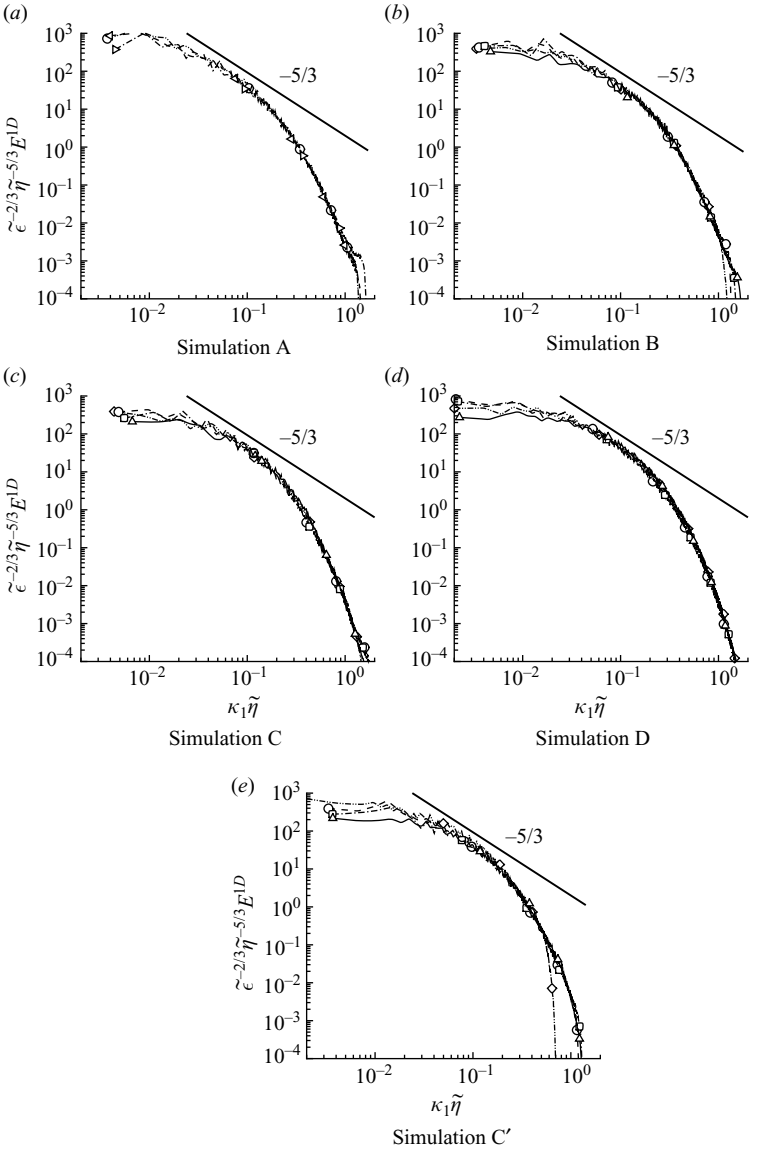

FIGURE 5. Energy spectra at different planes across the shear layer at the end of simulations. P_0 (○), P_1 (◁ for case A and ◇ for cases B, C, D and C′), P_2 (▷ for case A and △ for cases B, C, D and C′) and P_s (□).

We remark that plane P_1 of case C′ is somewhat less resolved than other planes and the other simulations. This is observed in the dissipation subrange of plane P_1 (see figures 5*e* and 7*e*) where only the first 2/3 of the subrange collapses to an exponential decay. This is also reflected in table 3 that lists $\eta_{min}/\Delta x$ as being half that of simulation C, the latter being well resolved. This is a limitation of the choice of parameters made for case C′ to attempt to match case C as closely as possible, in terms of the resolution and thermodynamic parameters, while keeping the Reynolds number high enough. A simulation with temperature-dependent viscosity that matched the cold Reynolds number of simulation C would have an effectively lower local turbulence Reynolds

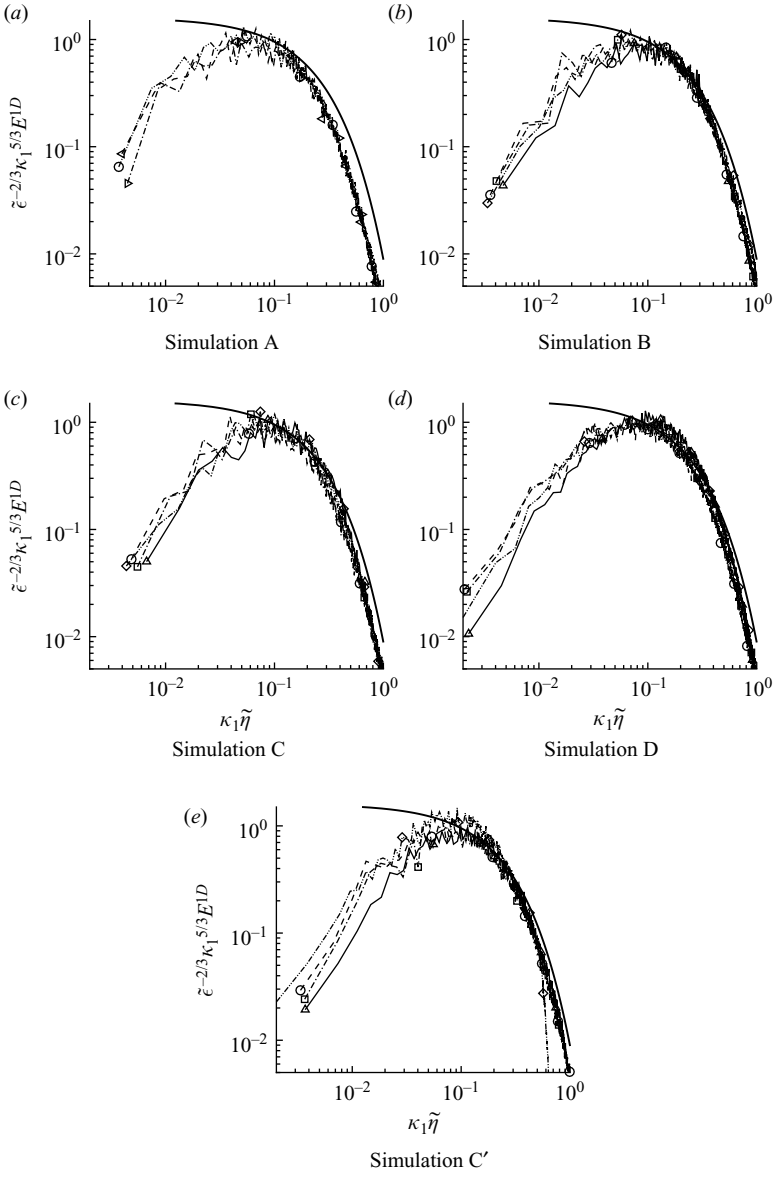

FIGURE 6. Compensated energy spectra in logarithmic coordinates at different planes across the shear layer at the end of simulations. P_0 (○), P_1 (◁ for case A and ◇ for cases B, C, D and C′), P_2 (▷ for case A and △ for cases B, C,D and C′) and P_s (□). Solid line is the theoretical spectrum given by (3.2).

number, across the shear layer, owing to the increase of viscosity caused by the increase in temperature induced by the combustion. The lower turbulence Reynolds number of such hypothetical simulation would have prevented close statistical comparison with the rest of the data analysed in this study. Therefore, the simulation parameters were chosen as a compromise between the resolution we could afford and the turbulence physics being investigated. This turned out to affect some of the statistics of the effectively high local Reynolds number side of the shear layer, i.e. the P_1 plane, while

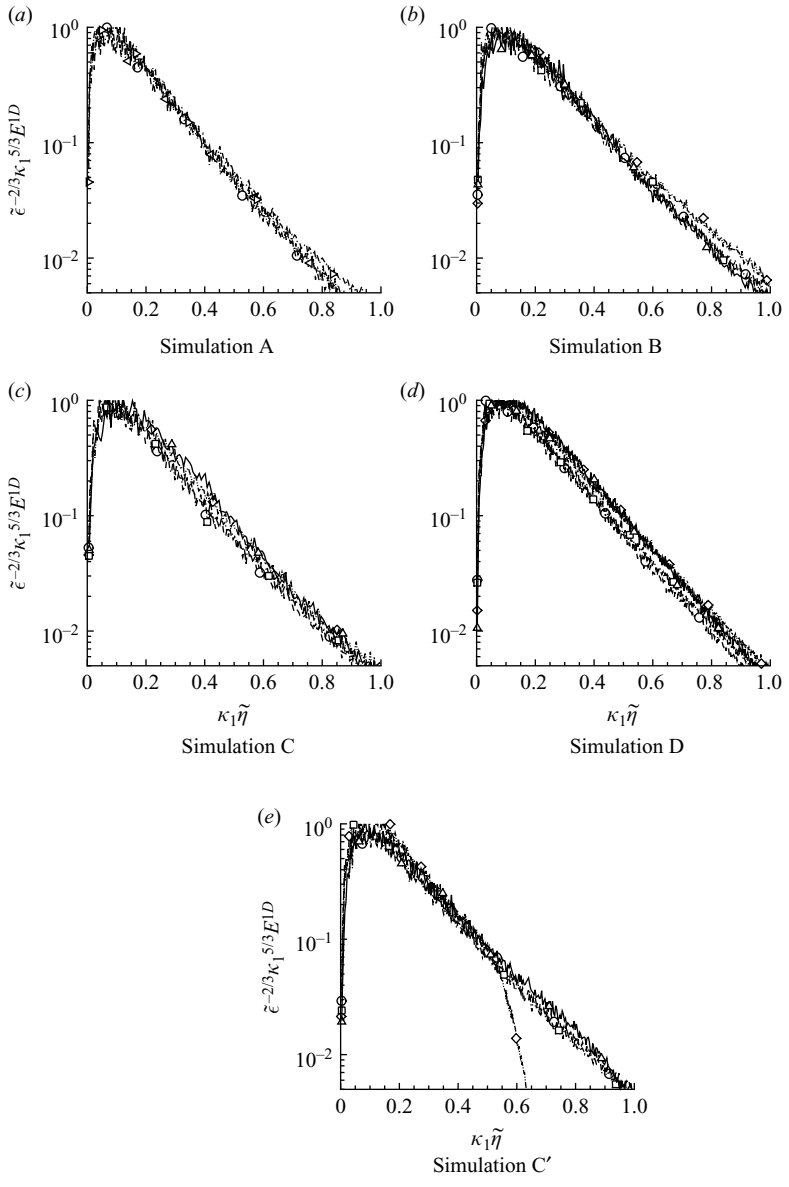

FIGURE 7. Compensated energy spectra in linear-logarithmic coordinates at different planes across the shear layer at the end of simulations. P_0 (○), P_1 (◁ for case A and ◇ for cases B, C, D and C′), P_2 (▷ for case A and △ for cases B, C, D and C′) and P_s (□).

the other planes appear to be well resolved. For these reasons, the results pertaining to plane P_1 of simulation C′ will be excluded from this point onwards.

3.2. *Mixture fraction spectra*

The mixture fraction spectrum $E_Z^{1D}(\kappa_1)$ has been normalized in agreement with the scaling (Tennekes & Lumley 1972)

$$E_Z^{1D} \propto \tilde{\chi}\tilde{\epsilon}^{-1/3}\kappa_1^{-5/3}\mathrm{e}^{-\beta_Z\kappa_1\tilde{\eta}}, \tag{3.3}$$

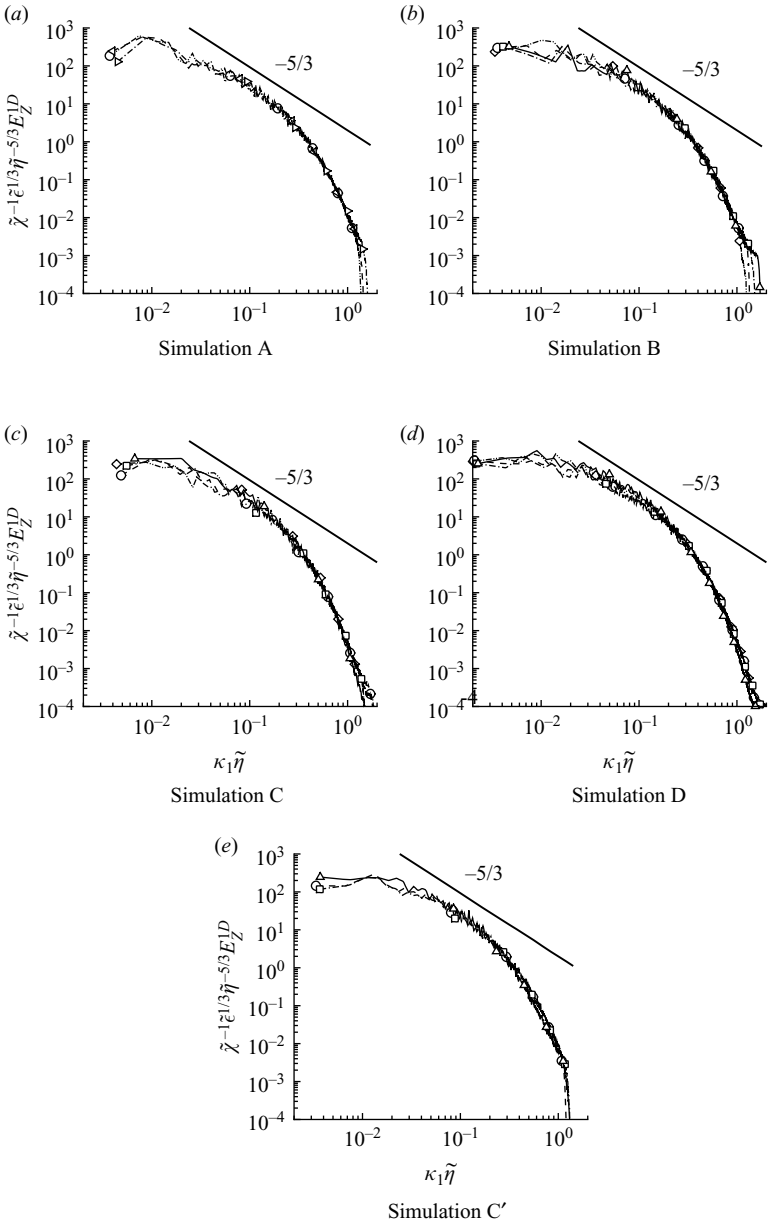

FIGURE 8. Mixture fraction spectra at different planes across the shear layer at the end of simulations. P_0 (○), P_1 (◁ for case A and ◇ for cases B, C, D and C′), P_2 (▷ for case A and △ for cases B, C, D and C′) and P_s (□).

where β_Z is the roll-off constant for the mixture fraction. Figure 8 shows the normalized spectra and figure 9 shows the compensated spectra from all simulations at all planes across the shear layer. In general, the behaviour of the mixture fraction spectrum is very similar to that of the turbulence energy spectrum, even in the cases with substantial heat release. In all simulations, the Schmidt number is close to unity ($Sc = 1$ in case A and 0.7 in all reacting cases) and therefore use of the Kolmogorov scale instead of the Obukhov–Corrsin scale has a negligible impact on the plots.

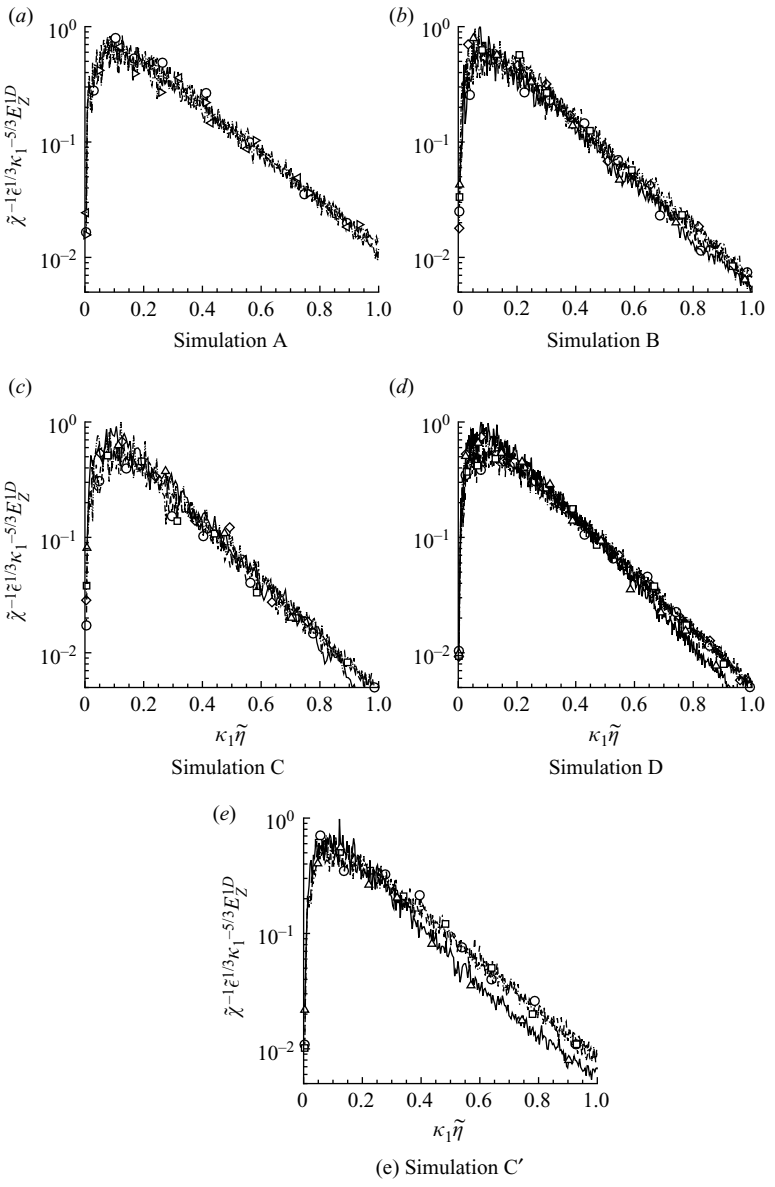

FIGURE 9. Compensated mixture fraction spectra in linear-logarithmic coordinates at different planes across the shear layer at the end of simulations. P_0 (○), P_1 (◁ for case A and ◇ for cases B, C, D and C′), P_2 (▷ for case A and △ for cases B, C, D and C′) and P_s (□).

A scaling similar to that of the energy spectrum is supported by a large body of experimental and computational results in incompressible flows. The $-5/3$ scaling has been observed previously in the temperature field of gas-phase turbulent jets (Dowling & Dimotakis 1990; Dowling 1991) and in jet flames (Wang *et al.* 2005; Nagel & Dahm 2007). Inertial scaling is suggested in experiments by Dowling & Dimotakis (1990) and Su & Clemens (2003), even at Reynolds numbers as low as 3000, and by many others. Similar results are suggested by others using DNS of passive (Overholt & Pope 1996) and active (de Bruyn Kops *et al.* 2001) scalars. We

observe little difference between non-reacting and reacting cases when the spectrum is normalized using Favre-averaged quantities. The same behaviour is observed for the compensated spectrum in figure 9, with results that are completely analogous to those previously discussed for the energy spectrum.

3.3. *Velocity–mixture fraction cospectra*

We conclude this section with the analysis of the spectra of the turbulent fluxes, $C^{1D}_{u_1Z}$, $C^{1D}_{u_2Z}$ and $C^{1D}_{u_1u_2}$, between velocity and mixture fraction. In the temporal shear layer, only the streamwise and the vertical velocity components lead to non-zero turbulent fluxes. Cross-spectra with the spanwise velocity component is negligible owing to the homogeneity of the flow in that direction. In our simulations Q_{u_iZ} appeared to be practically zero and it was not possible to ascertain its magnitude from the simulation data. Note that Q_{u_iZ} is zero for a scalar in isotropic turbulence (O'Gorman & Pullin 2003).

Lumley (1967) predicted that, by similarity analysis, the cospectrum of a passive scalar mixing in a homogeneous turbulent field in the presence of mean scalar gradient takes the form

$$C^{1D}_{u_1Z} \propto -S_Z \tilde{\epsilon}^{1/3} \kappa_1^{-7/3}, \tag{3.4}$$

in the inertial-convective subrange, where S_Z is the mean scalar gradient. Experimental measurements by Mydlarski & Warhaft (1998) investigated the one-dimensional velocity–temperature cospectrum and found a wavenumber dependence of approximately κ_1^{-2} for $Re_\lambda = 582$. Further experimental measurements in another study by Mydlarski (2003) in the range of $Re_\lambda = 85$ to 582 reveal a tendency towards the theoretical limit of Lumley as the Reynolds number increases. A purely passive scalar case was investigated by O'Gorman & Pullin (2003) who reported approximately $\kappa_1^{-7/3}$ scaling for Schmidt numbers of order unity by using sparse direct-interaction perturbation (Kida & Goto 1997) and closer to κ_1^{-2} from their DNS at $Re_\lambda = 265$. Finally, a recent EDQNM study by Bos, Touil & Bertoglio (2005) predicts that the asymptotic result of Lumley is achieved only at very high Reynolds numbers.

The majority of the referenced works on the turbulence flux cospectrum consider mixing of a scalar with a mean gradient in isotropic non-reacting turbulence. In the case of the shear layer, two mean gradients are present, one associated with the streamwise velocity S_u and a second associated with the mixture fraction S_Z. Therefore, for consistency, one should consider a spectrum scaling that is dependent not only on S_Z but also on S_u. Fortunately, for the case of the shear layer, these two quantities are essentially indistinguishable, with $S_Z \approx S_u/\Delta u \approx S$ at all times, except during the initial non-turbulent transient stage of the evolution of the shear layer which is not of interest at present. Figures 10, 11 and 12 show normalized cospectra for all the simulations at all the planes considered which supports the conjecture that a single mean gradient is relevant in the scaling. It is observed that the profiles collapse to some degree in the middle of the wavenumber range but there is too much statistical variability as the wavenumber increases to ascertain their behaviour. Nevertheless, it is observed that the profiles are very similar in all cases, reactive and non-reactive simulations, and the large density variations in these flows are not sufficient to affect the normalized spectra. There is some degree of variability among the case, which we attribute to the differences in Reynolds numbers between cases. Note that the statistical convergence of the cospectra is lower than that of the autospectra discussed in the previous sections. At high wavenumbers, the cospectra

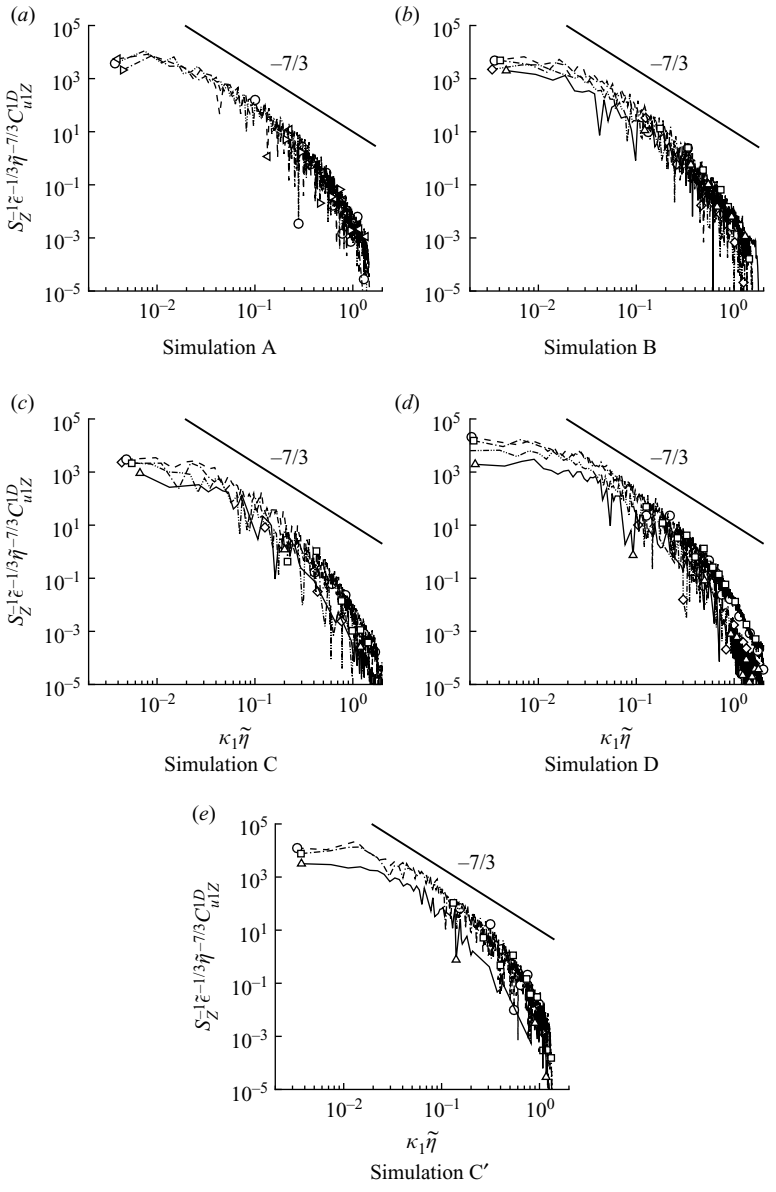

FIGURE 10. Cospectra $C_{u_1Z}^{1D}$ at different planes across the shear layer at the end of simulations. Solid line corresponds with $\kappa^{-7/3}$ in the inertial-convective subrange. P_0 (○), P_1 (◁ for case A and ◇ for cases B, C, D and C′), P_2 (▷ for case A and △ for cases B, C, D and C′) and P_s (□).

were not sufficiently converged to ensure positive values of the normalized profiles, and this shows as missing data points in the plots.

Figures 13, 14 and 15 show compensated cospectra for all the simulations. This representation accentuates the middle of the wavenumber range. As in the case of the turbulence energy spectra, the profiles curve gradually and it is not possible to infer unequivocally the presence of a $\kappa_1^{-7/3}$ inertial-convective subrange. This is consistent with the experimental evidence suggesting that the asymptotic scaling is present only at higher Reynolds numbers than those considered in the present simulations.

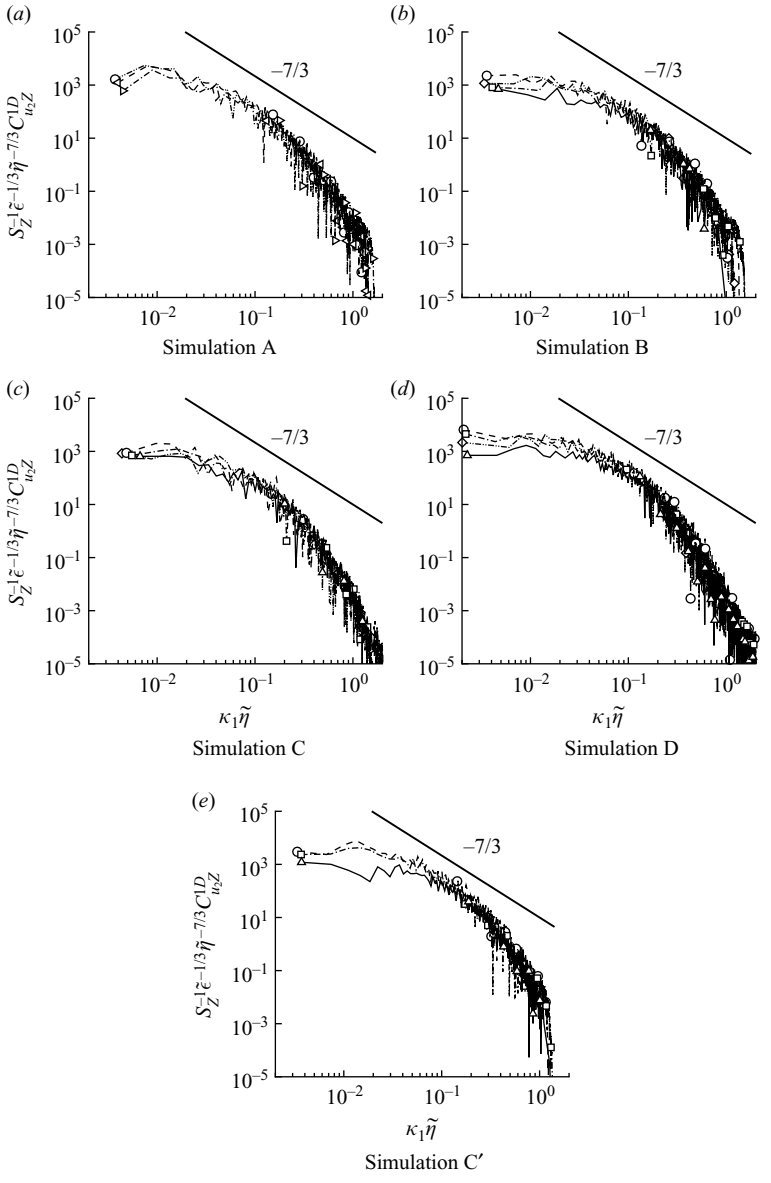

FIGURE 11. Cospectra $C^{1D}_{u_2Z}$ at different planes across the shear layer at the end of simulations. Solid line corresponds with $\kappa_1^{-7/3}$ in the inertial-convective subrange. P_0 (○), P_1 (◁ for case A and ◇ for cases B, C, D and C′), P_2 (▷ for case A and △ for cases B, C, D and C′) and P_s (□).

4. Temperature

The statistics of the temperature field are of particular importance in reacting flows as temperature couples with radiation and other heat transfer phenomena in combustion processes. In the reacting fast chemistry limit and assuming unit Lewis number (equal diffusivity and heat conduction) and low Mach number, the temperature can be related to the mixture fraction uniquely by a so-called state function $T = T^e(Z)$. This relationship is obtained from the energy equation of this two-stream system by neglecting pressure variations and viscous dissipation throughout

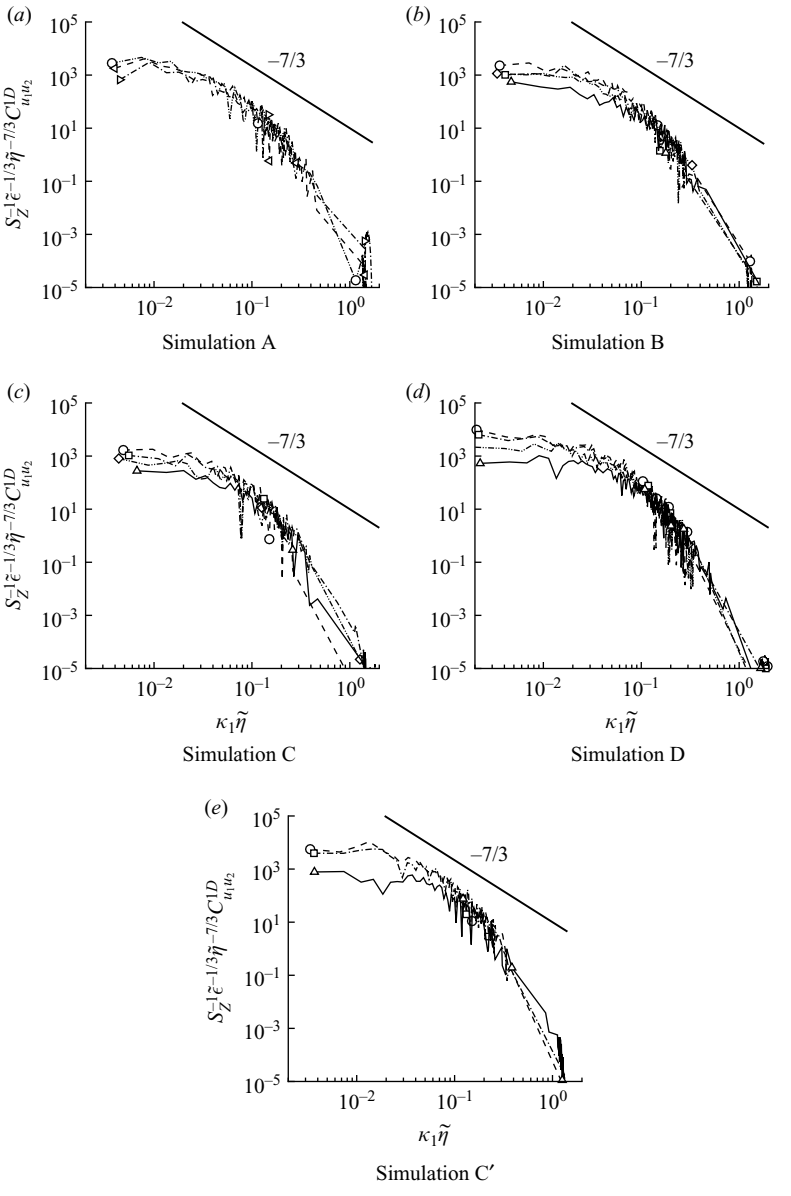

FIGURE 12. Cospectra $C^{1D}_{u_1u_2}$ at different planes across the shear layer at the end of simulations. Solid line corresponds with $\kappa_1^{-7/3}$ in the inertial-convective subrange. P_0 (○), P_1 (◁ for case A and ◇ for cases B, C, D and C′), P_2 (▷ for case A and △ for cases B, C, D and C′) and P_s (□).

the flow, giving

$$h = \sum_{i=1}^{N} Y_i(Z)h_i(T) = \sum_{i=1}^{N} Y_i(Z)\left(\Delta h_i^o + \int_1^T C_{pi}(T')\mathrm{d}T'\right) = h_o + (h_f - h_o)Z, \quad (4.1)$$

where N is the total number of species in the gas mixture, and h_o and h_f denote the enthalpy of the oxidizer and fuel streams, respectively. This equation defines $T^e(Z)$,

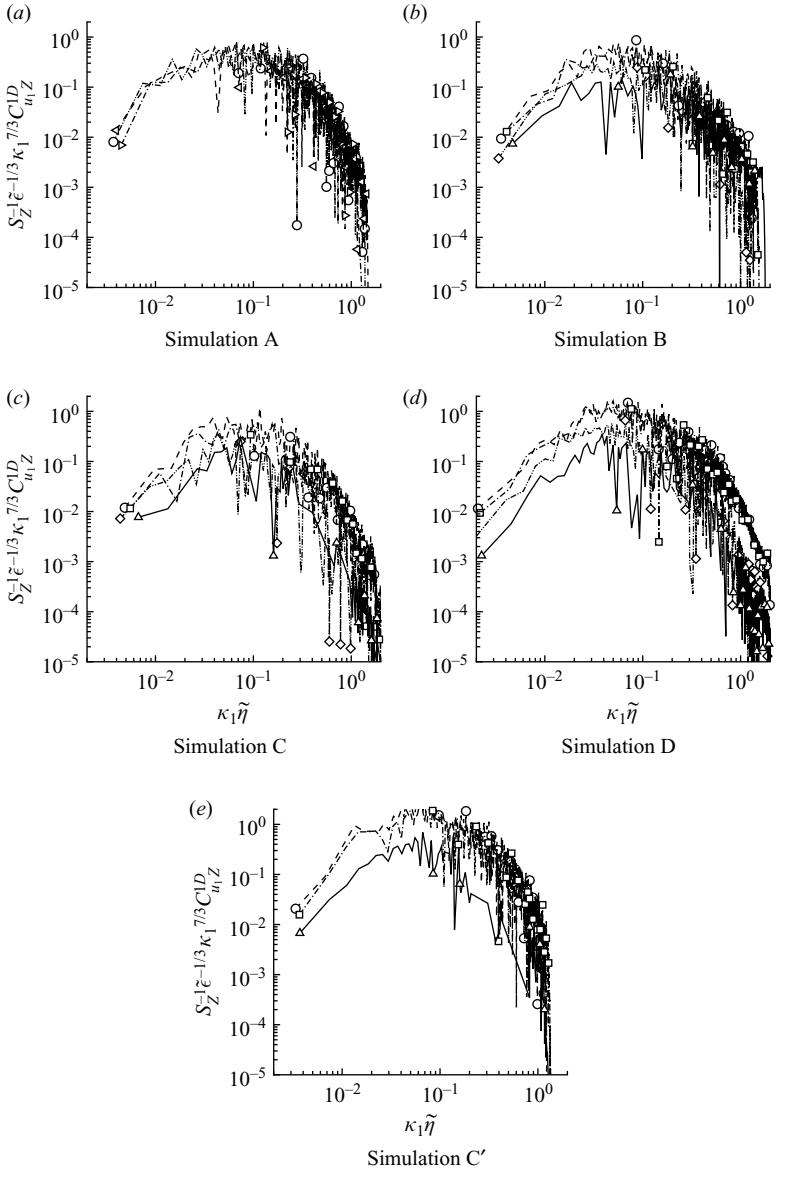

FIGURE 13. Compensated $C_{u_1Z}^{1D}$ cospectra in logarithmic coordinates at different planes across the shear layer at the end of simulations. Solid line corresponds with $\kappa^{-7/3}$ in the inertial-convective subrange. P_0 (○), P_1 (◁ for case A and ◇ for cases B, C, D and C′), P_2 (▷ for case A and △ for cases B, C, D and C′) and P_s (□).

which at $Z = Z_s$ gives the adiabatic flame temperature T_f. This nonlinear function, shown in figure 16 for all simulations, depends on the free-stream composition and thermodynamic properties of the mixture (Williams 1985).

It will be convenient in follow-up developments to consider a simplified piecewise linear approximation to (4.1) that exposes explicitly the dependence of the temperature

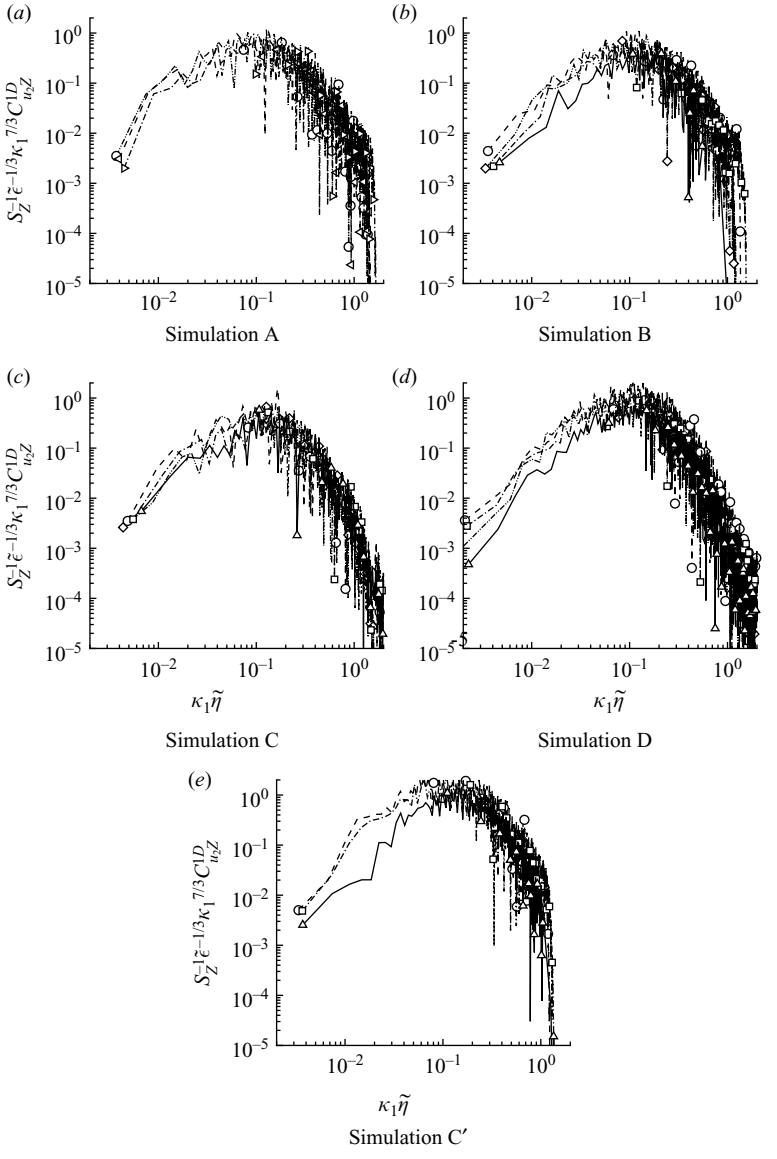

FIGURE 14. Compensated $C_{u_2Z}^{1D}$ in logarithmic coordinates at different planes across the shear layer at the end of simulations. Solid line corresponds with $\kappa_1^{-7/3}$ in the inertial-convective subrange. P_0 (○), P_1 (◁ for case A and ◇ for cases B, C, D and C′), P_2 (▷ for case A and △ for cases B, C, D and C′) and P_s (□).

on the mixture fraction. The general relationship is implicitly defined by (4.1) but it can be simplified to

$$T^e(Z) = \begin{cases} 1 + \bar{Q}\phi Z & Z \leqslant Z_s, \\ 1 + \bar{Q}(1-Z) & Z > Z_s, \end{cases} \tag{4.2}$$

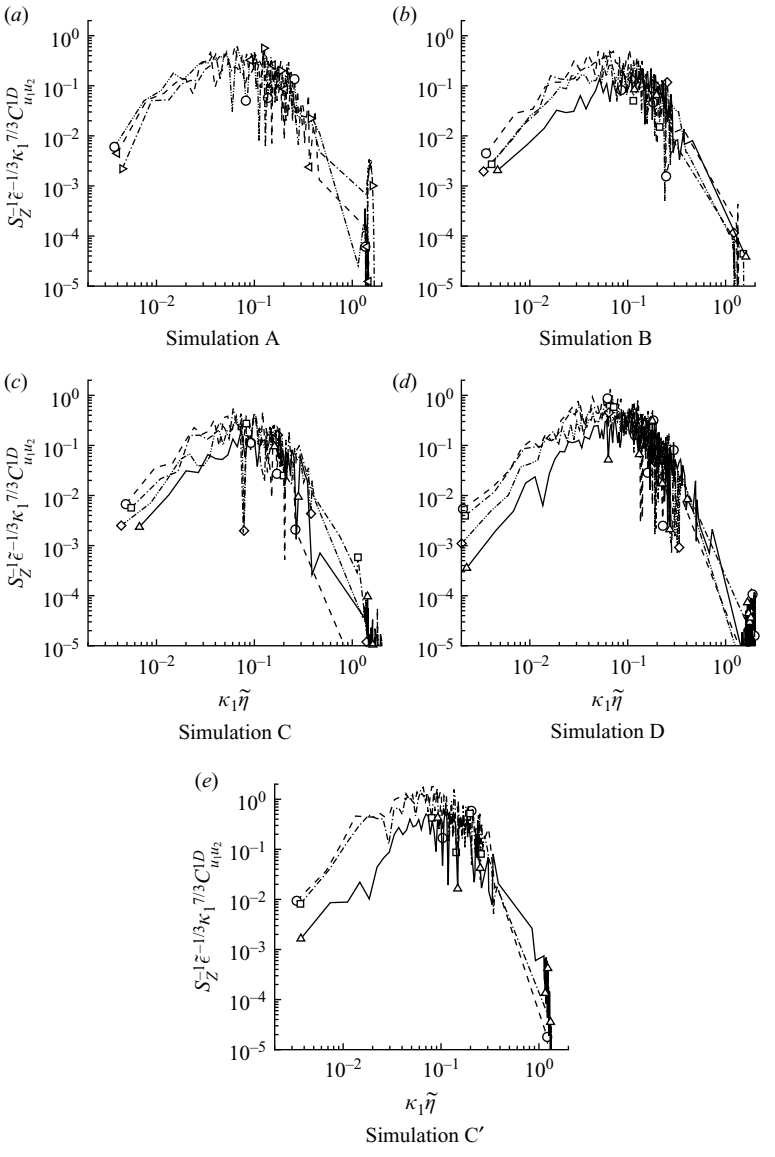

FIGURE 15. Compensated $C_{u_1u_2}^{1D}$ in logarithmic coordinates at different planes across the shear layer at the end of simulations. Solid line corresponds with $\kappa_1^{-7/3}$ in the inertial-convective subrange. P_0 (○), P_1 (◁ for case A and ◇ for cases B, C, D and C′), P_2 (▷ for case A and △ for cases B, C, D and C′) and P_s (□).

where $\bar{Q}$ is the average heat release parameter obtained by defining average specific heats according to

$$\bar{C}_{pi} = \frac{1}{T_f - 1}\int_1^{T_f} C_{pi}(T')\mathrm{d}T', \tag{4.3}$$

giving

$$\bar{Q} = \frac{h_o + (h_f - h_o)Z_s - \sum_{i=1}^{N} Y_i(Z_s)\Delta h_i^o}{\phi Z_s \sum_{i=1}^{N} Y_i(Z_s)\bar{C}_{pi}}. \tag{4.4}$$

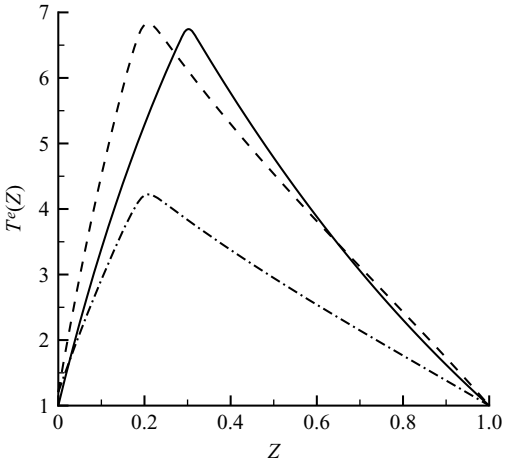

FIGURE 16. Normalized temperature state relationship $T = T^e(Z)$, (4.1), for case B (dash-dot line), case C and C′ (dashed line) and case D (solid line).

A small error is introduced by this approximation when taking the temperature of the free streams to be equal to 1 in simulations B, C and C′. This error is between 2.5 % and 4 % of the adiabatic flame temperature in these simulations and is within the approximation error introduced by using the average heat release parameter $\bar{Q}$ of (4.4) in (4.2).

4.1. *Temperature variance*

The temperature spectra, which were not discussed in the previous sections, contain the information of the two-point statistics, length scales, of the temperature fluctuations T'. The average of the spectra equals to the Reynolds-averaged temperature variance $\overline{T'^2}$. It is common to neglect distinguishing between $\overline{T'^2}$ and the Favre-averaged temperature variance $\widetilde{T''^2}$ when discussing the spectra of T' since the transport equation of $\widetilde{T''^2}$ has a more convenient form in variable-density flows. The difference between the Reynolds and Favre-averaged variances is

$$\widetilde{T''^2} = \overline{T'^2} + \frac{\overline{\rho' T'^2}}{\bar{\rho}} - \left(\frac{\overline{\rho' T'}}{\bar{\rho}}\right)^2. \tag{4.5}$$

The last two terms in the right-hand side of (4.5) are not generally zero. In our simulations, the peak $\widetilde{T''^2}$ is larger than $\overline{T'^2}$ by approximately 11 %, 15 % and 20 % for cases B, C and D, respectively. Therefore, this implies that a small inconsistency is introduced when the spectra of T' is normalized with Favre-averaged statistics. This is in part unavoidable because the rate of dissipation, which is utilized in the scalings, of $\overline{T'^2}$ has expressions and interpretations that are not as convenient and unequivocal as the Favre-averaged counterparts for variable-density flows. This problem also affects the turbulence energy and mixture fraction spectra discussed in the previous sections, but given the level of statistical noise in the profiles and narrow range of Reynolds number of the flows it is not possible to appreciate an effect in the figures. Therefore, from this point onwards we will consider the spectra of T' scaled on statistics deduced from $\widetilde{T''^2}$, since a more consistent approach has yet to be developed.

An expression for the rate of dissipation of temperature fluctuations, χ_T, needs to be obtained in order to derive scaling statistics for the reacting flows considered in

this study. The value of χ_T is related to the rate of dissipation of mixture fraction χ, since $T = T^e(Z)$. Everest *et al.* (1995) defines χ_T such that it is analogous to χ, according to

$$\chi_T = 2D\nabla T \cdot \nabla T = 2D\nabla Z \cdot \nabla Z \left(\frac{\mathrm{d}T^e}{\mathrm{d}Z}\right)^2 = \chi \left(\frac{\mathrm{d}T^e}{\mathrm{d}Z}\right)^2, \tag{4.6}$$

where D is the diffusion coefficient of the mixture fraction. Equation (4.6) neglects the contribution to χ_T from the average temperature profile, which is small at high Reynolds numbers. One question to be answered is whether this is the only quantity responsible for the destruction of temperature fluctuations under the infinitely-fast-chemistry approximation. This matters because of its relationship to the length scales of the temperature field.

Let us consider the conservation equation for $\widetilde{T''^2}$, which can be obtained from the conservation equation for the mixture fraction, given by

$$\rho \frac{DZ}{Dt} = \nabla \cdot (\rho D \nabla Z). \tag{4.7}$$

Now, multiply (4.7) by the derivative of $T^e(Z)$ with respect to Z to obtain

$$\rho \frac{\mathrm{d}T^e}{\mathrm{d}Z}\frac{DZ}{Dt} = \rho \frac{DT}{Dt} = \frac{\mathrm{d}T^e}{\mathrm{d}Z}\nabla \cdot (\rho D \nabla Z). \tag{4.8}$$

Rearranging the right-hand side gives

$$\rho \frac{DT}{Dt} = \nabla \cdot (\rho D \nabla T) - \frac{1}{2}\rho\chi \frac{\mathrm{d}^2 T^e}{\mathrm{d}Z^2}, \tag{4.9}$$

where the last term is analogous to the result derived by Bilger (1980) relating the rate of production of species to the scalar dissipation in the infinitely fast chemistry case. Note that the last term in (4.9) is not zero, even if T is a piecewise linear function of Z, because the curvature of the temperature profile in mixture fraction space is very large at the stoichiometric surface, e.g. infinitely large in the infinitely fast chemistry limit. This equation can then be used to derive the conservation equation for $\widetilde{T''^2}$ by the usual manipulation, giving

$$\begin{aligned}\frac{\partial}{\partial t}(\bar{\rho}\widetilde{T''^2}) + \frac{\partial}{\partial x_k}\left(\bar{\rho}\tilde{u}_k\widetilde{T''^2}\right) = {} & -2\bar{\rho}\widetilde{u_k''T''}\frac{\partial \tilde{T}}{\partial x_k} - \frac{\partial}{\partial x_k}\left(\bar{\rho}\widetilde{u_k''T''^2} + \overline{2\rho D T''\frac{\partial T}{\partial x_k}}\right) \\ & - \bar{\rho}\tilde{\chi}_T - \overline{\rho\chi T''\frac{\mathrm{d}^2 T^e}{\mathrm{d}Z^2}}.\end{aligned} \tag{4.10}$$

The last term appearing on the right-hand side of (4.10) is not present in the analogous equation for the enthalpy variance $\widetilde{h''^2}$ since h is a linear function of Z (see (4.1)). Moreover, all the terms in (4.10) are present in the case of a passive scalar except the last, which we chose to denote by

$$\bar{\rho}\tilde{\chi}_T^e = \overline{\rho\chi T''\frac{\mathrm{d}^2 T^e}{\mathrm{d}Z^2}}. \tag{4.11}$$

Negative $\tilde{\chi}_T^e$ implies a decreased rate of temperature variance dissipation, i.e. relative production of temperature fluctuations. In flows at high Reynolds numbers, χ and T'' are usually not strongly correlated but the large temperature curvature term at the stoichiometric surface can lead to an overall average that is comparable to $\tilde{\chi}_T$. This is true only if the probability of crossing the stoichiometric surface is high at

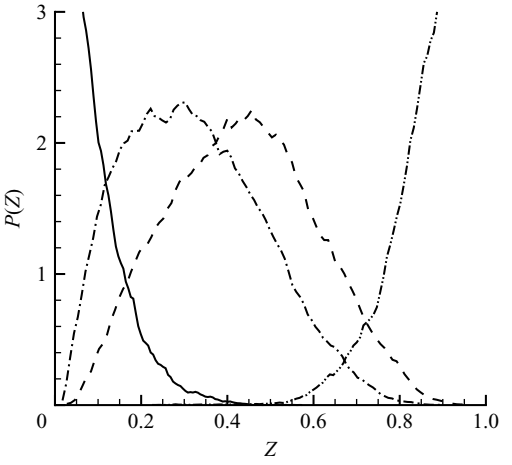

FIGURE 17. The p.d.f. of the mixture fraction for case D at plane P_0 (dashed line), P_1 (solid line), P_2 (dash-dot-dot line) and P_s (dash-dot line).

the considered plane where averages are computed. Theoretically, both $\tilde{\chi}_T^e$ and $\tilde{\chi}_T$ can be fully determined using the Favre joint p.d.f. of mixture fraction and scalar dissipation, $\tilde{P}(Z, \chi)$, according to

$$\tilde{\chi}_T = \int_0^1 \int_0^\infty \chi \left(\frac{\mathrm{d}T^e}{\mathrm{d}Z}\right)^2 \tilde{P}(Z, \chi)\, \mathrm{d}\chi \mathrm{d}Z = \int_0^1 \left(\frac{\mathrm{d}T^e}{\mathrm{d}Z}\right)^2 \langle \chi | Z \rangle \tilde{P}(Z)\, \mathrm{d}Z, \tag{4.12}$$

and

$$\tilde{\chi}_T^e = \int_0^1 \int_0^\infty \chi (T^e(Z) - \tilde{T}) \frac{\mathrm{d}^2 T^e}{\mathrm{d}Z^2} \tilde{P}(Z, \chi)\, \mathrm{d}\chi \mathrm{d}Z = \int_0^1 (T^e(Z) - \tilde{T}) \frac{\mathrm{d}^2 T^e}{\mathrm{d}Z^2} \langle \chi | Z \rangle \tilde{P}(Z)\, \mathrm{d}Z, \tag{4.13}$$

where $\tilde{P}(Z)$ is the one-point Favre p.d.f. of Z and $\langle \chi | Z \rangle$ denotes the average scalar dissipation conditioned on Z. In (4.13), the Favre average temperature is determined from

$$\tilde{T} = \int_0^1 T^e(Z) \tilde{P}(Z)\, \mathrm{d}Z. \tag{4.14}$$

For simplicity, distinction between the state-space variables associated with Z and χ in (4.12)–(4.14) is not made explicitly, but it is understood that the integration takes place in state-space. Moreover, for notational simplicity, the dependence of $\tilde{P}(Z)$ on x_2 is implicitly assumed and it is not shown. Equations (4.12) and (4.13) reflect the fact that the statistics of T are fully specified by those of Z and its derivatives. For future reference, figure 17 shows the Reynolds-based p.d.f. of mixture fraction (i.e. not remarkably different from the Favre-based p.d.f. in our simulations) at different planes for simulation D. The Favre and Reynolds p.d.f. for cases A, B and C are discussed in Pantano *et al.* (2003).

Assuming an infinitely thin reaction sheet, it is possible to show that $\tilde{\chi}_T^e$, as defined by (4.13), is always negative. Using (4.2) and (4.13) gives

$$\begin{aligned} \tilde{\chi}_T^e &= -\bar{Q}(\phi + 1) \int_0^1 (T^e(Z) - \tilde{T}) \delta(Z - Z_\mathrm{s}) \langle \chi | Z \rangle \tilde{P}(Z)\, \mathrm{d}Z \\ &= -\bar{Q}(\phi + 1)(T_\mathrm{f} - \tilde{T}) \langle \chi | Z_\mathrm{s} \rangle \tilde{P}(Z_\mathrm{s}) < 0, \end{aligned} \tag{4.15}$$

since χ, $(T_f - \tilde{T})$ and $P(Z)$ are positive quantities.

Given that the statistics of T are determined completely from the statistics of Z and the $T^e(Z)$ relationship, since the latter is fixed for a particular flow and does not have a stochastic (randomness) component associated with it, it may be possible to think of $\tilde{\chi}_T$ and $\tilde{\chi}_T^e$ not as two independent terms in (4.10) but as a single effect on $\widetilde{T''^2}$. Under these assumptions an overall rate of dissipation, given by

$$\tilde{\chi}_T^* = \tilde{\chi}_T + \tilde{\chi}_T^e, \tag{4.16}$$

may be a convenient statistic to scale the temperature spectra. Note that if the temperature fluctuations are to behave according to physical expectation, production of fluctuations from the mean gradient terms, first term in the right-hand side of (4.10), should be balanced by a dissipative term corresponding to the overall $\tilde{\chi}_T^*$. Therefore, this term should be positive.

4.2. *Temperature dissipation length scales*

One difficulty when attempting to estimate the dissipation length scale of the temperature fluctuations is that there is no well-defined diffusion coefficient for T. Ideally, one would like to use the diffusion coefficient of the mixture fraction to deduce one for the temperature. For example, the scaling

$$\bar{\rho}\tilde{\chi} = 2\tilde{D}\overline{\rho(\nabla Z)^2}, \tag{4.17}$$

could be assumed to serve as a definition of $\tilde{D}$. Analogously, a temperature 'diffusion coefficient' $\tilde{D}_T^*$ could be defined from

$$\bar{\rho}\tilde{\chi}_T^* = 2\tilde{D}_T^*\overline{\rho(\nabla T)^2}. \tag{4.18}$$

The mean diffusion coefficients $\tilde{D}$ and $\tilde{D}_T^*$ could then be used to define a modified Schmidt number for the temperature, Sc_T, which is distinct from the well-defined Prandtl number, according to

$$Sc_T = Sc\frac{\tilde{D}}{\tilde{D}_T^*} = Sc\frac{\tilde{\chi}}{\tilde{\chi}_T^*}\frac{\overline{\rho(\nabla T)^2}}{\overline{\rho(\nabla Z)^2}}. \tag{4.19}$$

Then Sc_T can be used to relate the Kolmogorov scale with passive mixing theories for either the Obukhov–Corrsin scale when $Sc_T < 1$ or the Batchelor scale when $Sc_T > 1$. Using these analogies, the dissipation subrange temperature fluctuation length scale is given by

$$\tilde{\eta}_T = \begin{cases} \tilde{\eta} Sc_T^{-3/4} & Sc_T \leqslant 1, \\ \tilde{\eta} Sc_T^{-1/2} & Sc_T > 1. \end{cases} \tag{4.20}$$

Alternatively, a spectral estimate of the dissipation length scale can be constructed according to

$$\tilde{\eta}_{T,\mathrm{sp}} = \frac{0.26}{\kappa_{1,peak}}, \tag{4.21}$$

where $\kappa_{1,peak}$ is the wavenumber of the peak of the dissipation spectrum $D_T^{1D} = 2D_T^*\kappa_1^2 E_T^{1D}$. This estimate is based on the observation that the scaled one-dimensional constant-density turbulence spectrum peaks at approximately $\kappa_1\eta \approx 0.26$ (Pope 2000). One advantage of (4.21) is that the actual value of D_T^* does not play a role in the resulting estimate.

Figure 18 shows Sc_T defined in (4.19) for all the simulations with heat release ($Sc_T = 1$ for case A). As can be seen, Sc_T increases around the mean stoichiometric plane in all cases. This implies smaller temperature length scales there, consistent

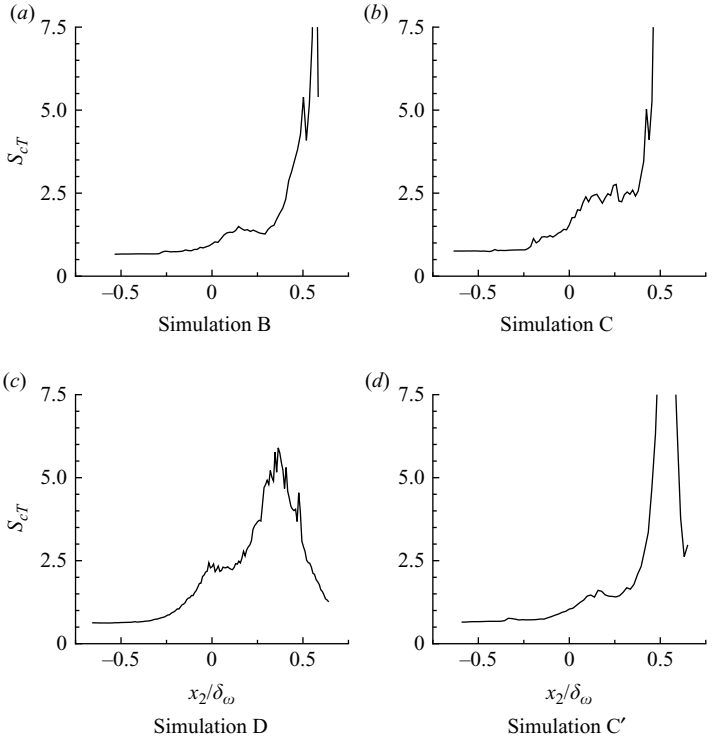

FIGURE 18. Temperature Schmidt number profiles across the shear layer for all cases.

Case	P_1	P_2	P_0	P_s
B	1.85	2.16	1.44	1.53
C	2	2	1.3	1.18
C′	2.16	1.73	1.3	1.18
D	2.16	2.16	1.3	1.3

TABLE 4. Temperature dissipation length scale based on the spectral estimate $\tilde{\eta}_{T,sp}$ normalized with $\tilde{\eta}$.

with recent experimental results (Wang *et al.* 2008). Figure 19 shows the temperature dissipation scale obtained through the passive scalar mixing analogy $\tilde{\eta}_T$ and the Kolmogorov scale $\tilde{\eta}$ for all cases. It is observed that the combined effect of heat release and variation of Sc_T leads to smaller length scales around the mean flame location plane. Finally, table 4 lists the values of the ratio $\tilde{\eta}_{T,sp}/\tilde{\eta}$ for all reactive flow simulations and the four planes investigated in this study. It is observed that the P_0 and P_s planes have consistently smaller values of $\tilde{\eta}_{T,sp}$ with respect to $\tilde{\eta}$. This is consistent with previous experimental observations (Kaiser & Frank 2007; Frank & Kaiser 2008; Wang & Barlow 2008; Wang *et al.* 2008).

4.3. *Temperature spectrum*

The temperature spectrum calculated at planes close to the stoichiometric mixture fraction plane were observed to have a reduced roll-off in the dissipation range. This appears to be caused by a reduction in the characteristic length scale of the

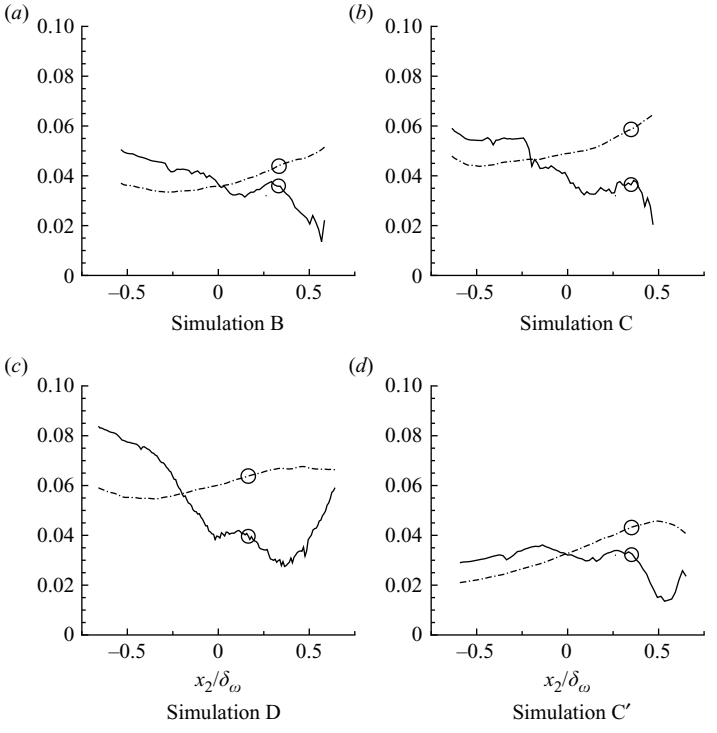

FIGURE 19. Temperature dissipation scale profiles across the shear layer for all cases. Continuous line denotes $\tilde{\eta}_T$ and dash-dotted line denotes $\tilde{\eta}$.

temperature fluctuations owing to the effects of heat release. By analogy with (3.3), the temperature spectrum could be assumed to take the form

$$E_T^{1D} \propto \tilde{\chi}_T \tilde{\epsilon}^{-1/3} \kappa_1^{-5/3} \mathrm{e}^{-\beta_T \kappa_1 \tilde{\eta}}, \tag{4.22}$$

where $\tilde{\chi}_T$ is the rate of temperature fluctuation dissipation and β_T is an exponential roll-off constant. This expression is a direct analogue of the mixture fraction spectrum scaling and relies, implicitly, in the fact that $T = T^e(Z)$. Under these assumptions, it is hoped that the spectrum will be similar to that of the mixture fraction. Alternatively, one can use the temperature dissipation and length scales defined previously to scale the spectra according to

$$E_T^{1D} \propto \tilde{\chi}_T^* \tilde{\epsilon}^{-1/3} \kappa_1^{-5/3} \mathrm{e}^{-\beta_T \kappa_1 \tilde{\eta}_T}. \tag{4.23}$$

The scaling in (4.22) is used in figure 20 to show normalized temperature spectra for simulations B, C, D and C′ at all planes across the shear layer. The temperature spectra profiles appear to collapse reasonably well in the middle of the wavenumber range for all cases and at all planes using $\tilde{\chi}_T$ from (4.12). It is also observed that the profiles do not collapse well within the dissipation subrange and the curves obtained at different planes differ substantially. Figure 21 shows compensated temperature spectra in linear-logarithmic coordinates which help distinguish the different behaviours exhibited at the different planes for the same simulations. As can be seen, two sets of planes, P_1 and P_2, on one hand, and P_0 and P_s, on the other hand, exhibit different slopes in the dissipation subrange. The planes P_0 and P_s show a reduced decay rate, smaller scales, compared to the rate of decay of the mixture fraction spectra. Note that the difference in scales between T and Z implies that the temperature spectra at P_1 and

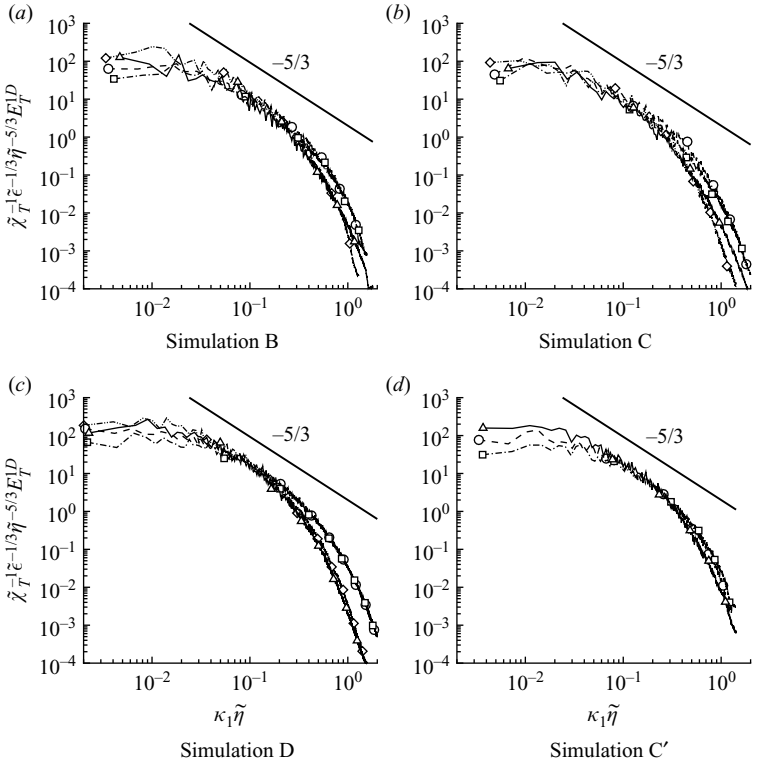

FIGURE 20. Temperature spectra at different planes across the shear layer at the end of simulations for planes P_0 (○), P_1 (◇), P_2 (△) and P_s (□).

P_2 are similar to those of the mixture fraction (whose profiles approximately collapse for all planes). In general, it appears that (4.22) is an accurate approximation of the functional form of the spectrum with a value of β_T that varies for different planes across the shear layer. It is possible to compensate for this effect by redefining a temperature length scale, akin to the Kolmogorov scale, which is mixture fraction dependent, and remove the apparent dependence of β_T on location in the turbulent flow. While possible, this will ruin the good collapse observed in the middle of the spectrum. That part of the spectrum does not appear to be affected to the same extent by heat release.

Figures 22 and 23 show normal and compensated spectra scaled according to (4.23). It is observed that both spectra collapse better using $\tilde{\chi}_T^*$ and η_T as the corresponding scales. The collapse using the new statistics is relatively good for all cases and planes but it is less satisfactory in the dissipation subrange of case D. Except in case D, the figures support our rationale for utilizing an overall rate of temperature fluctuations dissipation, $\tilde{\chi}_T^*$, as the relevant scaling quantity. In order to explore the reasons for the lack of collapse of the profiles in case D, an alternative approach is developed below which does not rely on the existence of analogies based on passive scalar mixing theories.

4.4. *Relationship between temperature and mixture fraction spectrum*

The relationship between the power-spectrum of a signal that is nonlinearly related to a second signal with known spectrum has a well-known mathematical treatment in signal processing (Thompson 1954; Shutterly 1963; Campbell 1964). This theory can

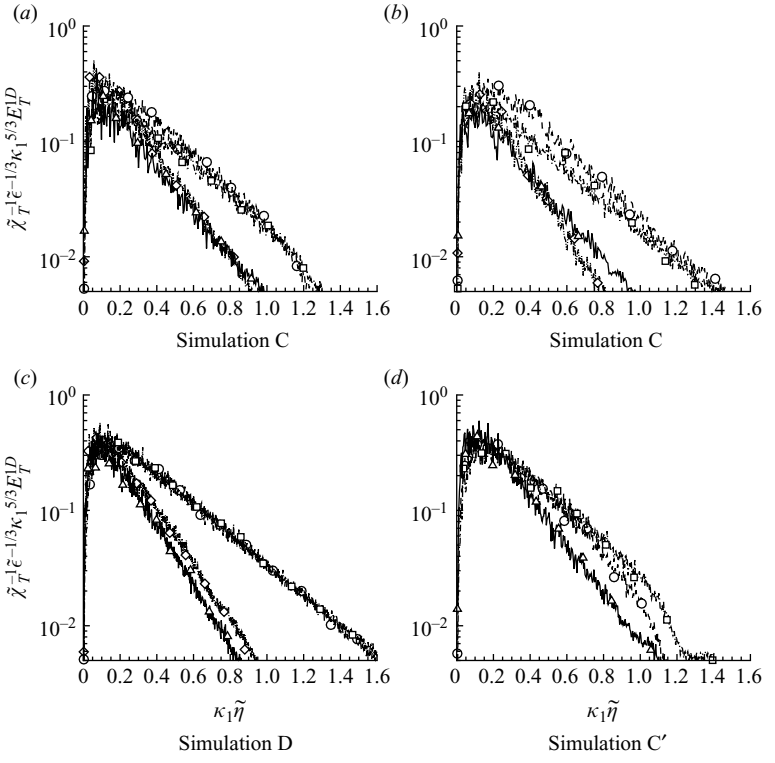

FIGURE 21. Compensated temperature spectra in linear-logarithmic coordinates at different planes across the shear layer at the end of simulations for planes P_0 (○), P_1 (◇), P_2 (△) and P_s (□).

be adapted with some modifications that incorporate the specific details of our case. As discussed by Shutterly (1963), the transformed spectrum can be expressed as an infinite series of the spectra of the moments of the original signal. First, the mixture fraction is decomposed into a mean and fluctuating component $Z(\boldsymbol{x}) = \overline{Z} + Z'(\boldsymbol{x})$, with $\bar{Z} = \overline{Z}(x_2)$ denoting the average component and $Z'(\boldsymbol{x})$ denoting the fluctuating component. For simplicity, we will omit the dependence of the fields on x_2 and time, since these parameters are fixed throughout the derivations that follow, and utilize Reynolds-averaged quantities. The one-dimensional correlation of the temperature is then given by the infinite sum

$$Re_T^{1D}(r_1) = \sum_{p,q,k,l=0}^{\infty} \frac{c_{pk}c_{ql}\overline{Z}^p\overline{Z}^q}{p!q!k!l!}\overline{Z'(\boldsymbol{x}+e_1r_1)^kZ'(\boldsymbol{x})^l}, \tag{4.24}$$

where

$$c_{pk} = \sum_{\nu=0}^{\infty} \alpha_\nu \overline{T^{e(p+k+\nu)}(Z)}, \tag{4.25}$$

with

$$\alpha_0 = 1, \quad \alpha_1 = -\overline{Z'} = 0, \quad \alpha_2 = -\frac{\overline{Z'^2}}{2!}, \quad \alpha_3 = -\frac{\overline{Z'^3}}{3!},$$

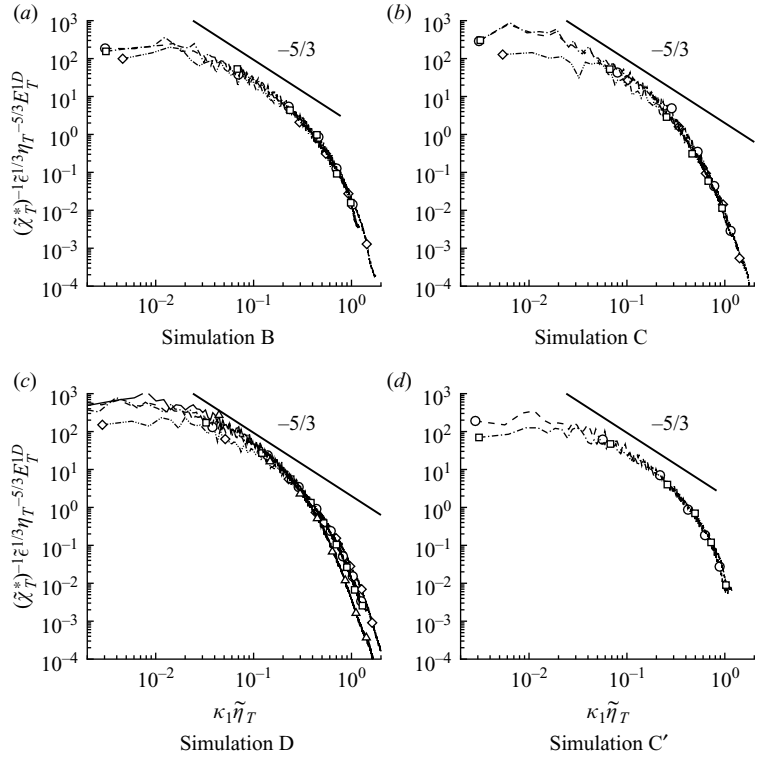

FIGURE 22. Temperature spectra at different planes across the shear layer at the end of simulations for planes P_0 (○), P_1 (◇), P_2 (△) and P_s (□). The profiles are normalized with $\tilde{\eta}_T$ and $\tilde{\chi}_T^*$.

$$\alpha_4 = -\frac{\overline{Z'^4}}{4!} + \frac{\overline{Z'^2}\ \overline{Z'^2}}{2!2!}, \quad \alpha_5 = -\frac{\overline{Z'^5}}{5!} + \frac{\overline{2Z'^3}\ \overline{Z'^2}}{3!2!}, \tag{4.26}$$

and for $\nu \geqslant 4$,

$$\alpha_\nu = -\frac{\overline{Z'^\nu}}{\nu!} + \sum_{r_1=1}^{\nu-1}\sum_{r_2=1}^{\nu-r_1}\frac{\overline{Z'^{r_1}}\ \overline{Z'^{r_2}}}{r_1!r_2!} - \sum_{r_1=1}^{\nu-2}\sum_{r_2=1}^{\nu-r_1-1}\sum_{r_3=1}^{\nu-r_1-r_2}\frac{\overline{Z'^{r_1}}\ \overline{Z'^{r_2}}\ \overline{Z'^{r_3}}}{r_1!r_2!r_3!} + \cdots + (-1)^\nu\overline{Z'}^\nu. \tag{4.27}$$

Using (4.24) and taking the Fourier transform term by term yields the temperature spectrum in terms of spectrum of moments of the mixture fraction,

$$E_T^{1D}(\kappa_1) = \sum_{p,q,k,l=0}^{\infty}\frac{c_{pk}c_{ql}\overline{Z}^p\overline{Z}^q}{k!p!q!l!}E_{kl}^{1D}(\kappa_1), \tag{4.28}$$

with

$$E_{kl}^{1D} = \frac{\overline{(\hat{\mu}_k\hat{\mu}_l^* + \hat{\mu}_k^*\hat{\mu}_l)}}{2} \quad \text{and} \quad \mu_k = Z'^k - \overline{Z'^k}. \tag{4.29}$$

The temperature spectrum can thus be considered as a weighted sum of various spectra, E_{kl}^{1D}, of the mixture fraction fluctuation moments. Note that it is likely possible

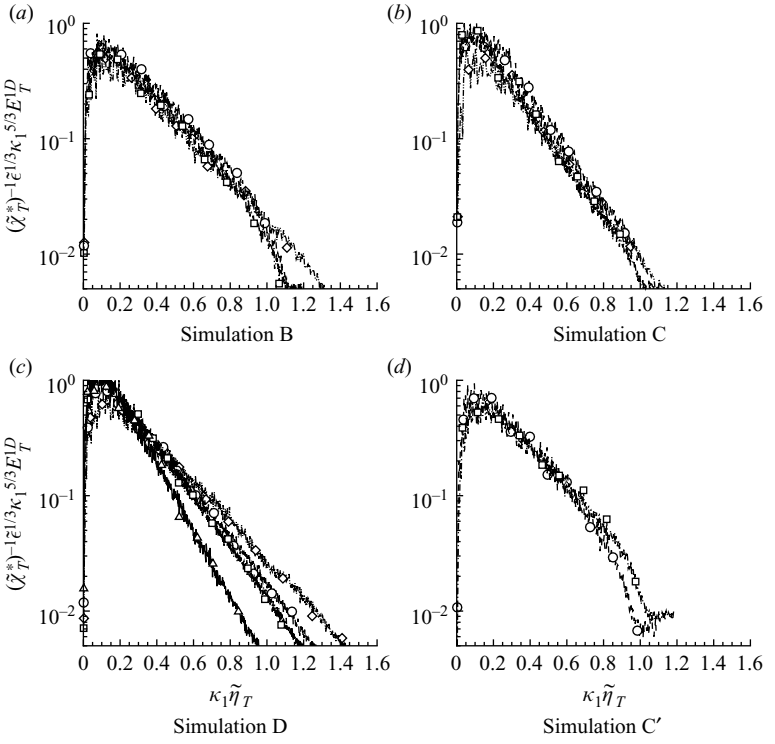

FIGURE 23. Compensated temperature spectra in linear-logarithmic coordinates at different planes across the shear layer at the end of simulations for planes P_0 (○), P_1 (◇), P_2 (△) and P_s (□). The profiles are normalized with $\tilde{\eta}_T$ and $\tilde{\chi}_T^*$.

to express E_{kl}^{1D} in terms of Fourier transform of the kl-order structure functions of Z'. This formulation was developed for the case of one-dimensional spectra but the same relationships apply for two- and three-dimensional spectra. This is the case because (4.28) expresses a relationship between spectra and remains valid independently of the power-spectrum being used, whether it is one-, two- or three-dimensional.

Considering the good collapse of the $E_Z^{1D} = E_{11}^{1D}$ spectra, shown in figure 8, the lack of collapse of the temperature spectra in the dissipation subrange is therefore a consequence of phase interactions of the Fourier modes of the mixture fraction moments. Moreover, the magnitude of the weights, (4.25), depend on the p.d.f. of mixture fraction $P(Z)$. Figure 24 shows the normalized moments of the mixture fraction fluctuation spectrum, which display similar behaviour to the E_Z^{1D} spectrum but with a slower decay in the dissipation subrange for the higher-order terms and a faster decay in the inertial subrange of the mixture fraction spectrum for all terms. A dimensionally based scaling of the E_{kl}^{1D} spectra based on the scalar dissipation, the turbulence dissipation and the wavenumber yields a $-(3+k+l)/3$ power-law of the spectrum in the inertial subrange, such that

$$E_{kl}^{1D} \propto \tilde{\chi}^{(k+l)/2}\tilde{\epsilon}^{-(k+l)/6}\kappa_1^{-(3+k+l)/3}. \tag{4.30}$$

As shown in figure 24, there is no good collapse of the data for moment spectrum with this scaling, except for the case $k = l = 1$ corresponding to (3.3). This is likely caused by phase interactions occurring between different moments of the mixture fraction fluctuations spectra.

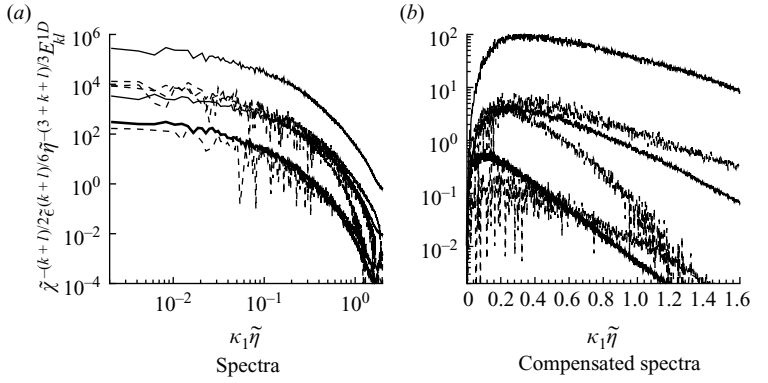

FIGURE 24. The moment mixture fraction spectra E_{kl}^{1D} with k and l between 1 and 3 in logarithmic coordinates (a) and in compensated form (b) for Case D plane P_0. Solid lines represent the diagonal terms and dashed lines represent the off-diagonal terms. The thicker solid line is the $E_Z^{1D} = E_{11}^{1D}$ spectrum.

Regardless of the scaling of E_{kl}^{1D}, it is now possible to reconstruct the temperature spectrum using (4.28). This requires either the analytical function $T = T^e(Z)$ (see figure 16) or an approximation to this expression. It was found that the series, (4.28), was not overly sensitive to the accuracy of the state relationship, and a piecewise linear approximation, (4.2), produced good results. Moreover, the derivative of (4.2) is discontinuous at the stoichiometric surface, $Z = Z_s$, which incidentally simplifies the evaluation of the integrals, (4.25), which reduces to

$$\overline{T^{e(n)}(Z)} = \int_{-\overline{Z}}^{1-\overline{Z}} T^{e(n)}(Z')P(Z')\,\mathrm{d}Z' = \int_0^1 T^{e(n)}(Z)P(Z)\,\mathrm{d}Z, \tag{4.31}$$

and gives the following expressions for the first four moments:

$$\overline{T(Z')} = \overline{T}, \tag{4.32}$$

$$\overline{T^{(1)}(Z')} = \bar{Q}\left((\phi+1)\int_0^{Z_s} P(Z)\,\mathrm{d}Z - 1\right), \tag{4.33}$$

$$\overline{T^{(2)}(Z')} = -\bar{Q}(\phi+1)\int_0^1 \delta(Z-Z_s)P(Z)\,\mathrm{d}Z = -\bar{Q}(\phi+1)P(Z_s), \tag{4.34}$$

$$\overline{T^{(3)}(Z')} = -\bar{Q}(\phi+1)\int_0^1 \delta^{(1)}(Z-Z_s)P(Z)\,\mathrm{d}Z = \bar{Q}(\phi+1)P'(Z_s). \tag{4.35}$$

It was found that only a few moments in (4.28) were required to recover an approximation of the temperature spectrum from the spectra of the moments of the mixture fraction. In the process of implementing these formulas it was found that the accuracy of the p.d.f. $P(Z)$ extracted from the simulations and shown in figure 17 was inadequate to prevent statistical noise from polluting the evaluation of the derivative required in (4.35). Therefore, a wavelet-based filtering of the p.d.f. was used to compute terms involving derivatives of the p.d.f. After these steps, it was found that the slope of the reconstructed spectrum did not change appreciably as additional terms in the expansion (4.28) were added. Note that in general the method calls for the $(p+k+\nu)$th derivative of the temperature state relation. By assuming a discontinuous state relation, the $(p+k+\nu-3)$th derivative of the probability distribution is needed to evaluate the truncated sums. It was observed

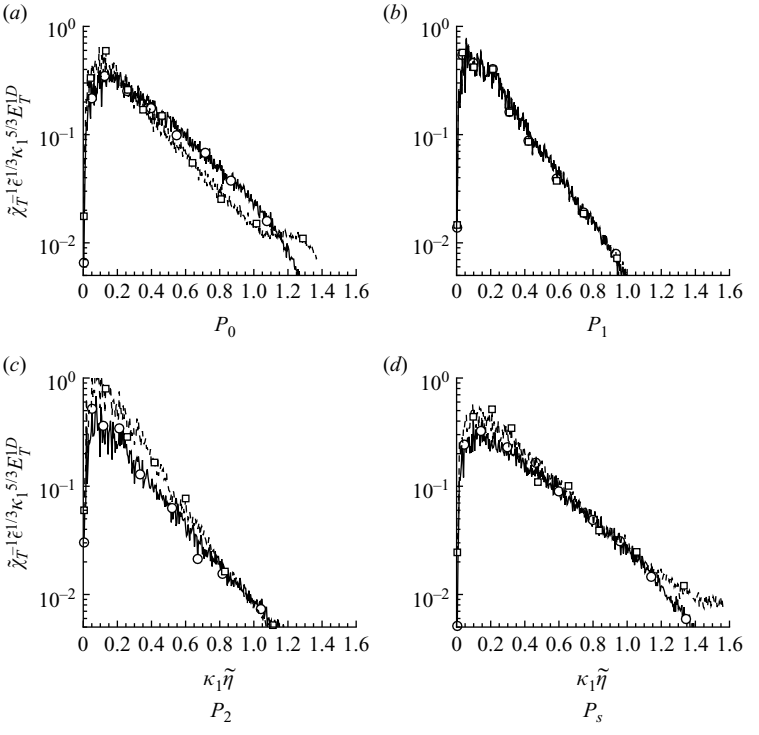

FIGURE 25. Reconstructed temperature spectra (○) from the mixture fraction spectra against the temperature spectra (□) at the four planes for Case B.

that the smaller dataset available in cases B, C and C′ contributed more error to these approximations and, in consequence, the reconstructed spectra suffered some degradation.

Figures 25–28 show the reconstructed and original compensated temperature spectra for all reactive cases at all planes considered across the shear layer. In particular, the spectra in the dissipation subrange of case D collapse relatively well. This is an improvement with respect to the approach discussed in the previous subsection using mixing analogies. Inspection of the relative importance of the different terms in (4.28) reveals that in the centre of the wavenumber range, the E_{11}^{1D} term dominates the sum, explaining why the temperature spectra seem to collapse well in that subrange when normalized with large-scale turbulent quantities. However, the spectra of the higher moments in the dissipation subrange cannot be neglected in the sum, leading to the slower decay observed in planes P_s and P_0 of figure 21. It is also observed that for those planes away from the centre of the shear layer, the contributions from the terms involving the derivatives of the p.d.f. are small. Correspondingly, the decay of the temperature spectrum in the dissipation subrange resembles that of the mixture fraction. Alternatively, for those planes close to the stoichiometric surface, the derivatives of the p.d.f. at the stoichiometric location are not small and this leads to larger contributions of the higher-order moment terms, which in turn leads to a reduced decay in the dissipation subrange. The change in the rate of decay of the spectrum closer to the flame sheet can thus be explained by enhanced contribution of higher moment terms in the sum, (4.28), and by a change

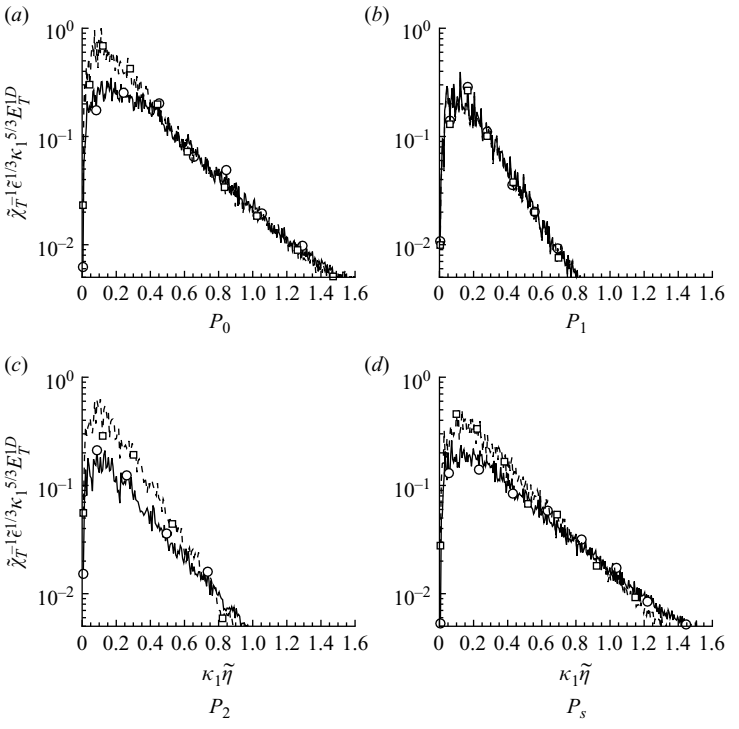

FIGURE 26. Reconstructed temperature spectra (○) from the mixture fraction spectra against the temperature spectra (□) at the four planes for Case C.

in the higher-order moment terms themselves owing to heat release. Both effects are observed here.

4.5. *Velocity–temperature cospectra*

The behaviour of the cospectra of temperature–velocity fluctuations in the middle of the wavenumber range is similar to that of the mixture fraction–velocity fluctuation cospectra. However, the same lack of collapse of the spectra in the dissipation subrange (taken at different planes across the shear layer) that was observed for the temperature autospectra is observed here. Figure 29 shows cospectra at all the planes considered for all reactive cases. The spectra have been non-dimensionalized using the scaling in (3.4) with the mixture fraction gradient replaced by the temperature gradient S_T according to

$$C_{u_1T}^{1D} \propto -S_T\tilde{\epsilon}^{1/3}\kappa_1^{-7/3}. \tag{4.36}$$

The analysis developed previously to relate the behaviour of the temperature autospectrum can also be generalized to address the behaviour of the cospectrum. An expansion similar to that leading to (4.24) shows that the velocity–temperature cross-spectra can be inferred from the two-point temperature–velocity cross-correlation according to

$$R_{u_iT}^{1D}(r_1) = \sum_{p,k=0}^{\infty} \frac{c_{pk}\overline{Z}^p}{p!k!}\overline{Z'(\boldsymbol{x}+e_1r_1)^k u_i'(\boldsymbol{x})}. \tag{4.37}$$

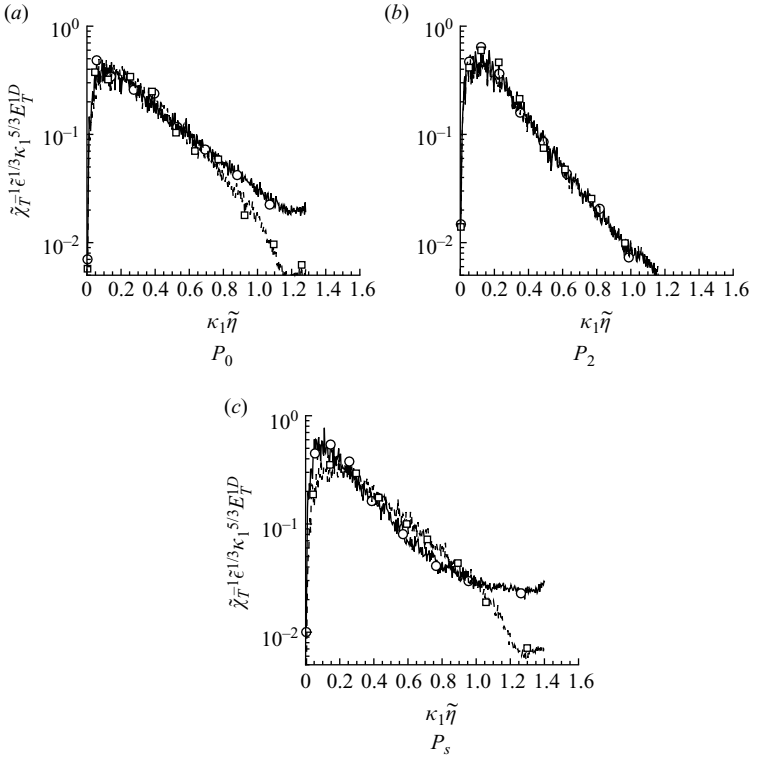

FIGURE 27. Reconstructed temperature spectra (○) from the mixture fraction spectra against the temperature spectra (□) at the four planes for Case C′.

This expression can then be used to determine the cospectrum, giving

$$F_{u_i T}^{1D}(\kappa_1) = \sum_{p,k=0}^{\infty} \frac{c_{pk}\overline{Z}^p}{p!k!}\overline{\hat{\mu}_k^*\hat{u}_i}. \tag{4.38}$$

As was discussed in § 3.3, the limited sampling of the simulation data contributed to substantially larger variability in the cospectra, as opposed to the better quality of the autospectra. In consequence, the reconstruction of the cospectra was not as accurate as that of the temperature autospectra and it is therefore not shown.

5. Conclusions

An analysis of the turbulence, mixture fraction and temperature spectra from DNS of turbulent non-premixed reacting shear layers under different levels of heat release (accomplished by varying dilution and fuels) using the infinitely-fast-chemistry limit is presented. In the case of the velocity and mixture fraction fields, the simulations show that scaling of the spectra based on Favre-averaged statistics, turbulence dissipation and scalar dissipation is able to collapse all the profiles across the shear layer quite well. This appears to apply in the middle of the wavenumber range and dissipation subranges of the spectra of all the simulations. This implies that when the effect of heat release is appropriately taken into account by the large-scale changes of the flow induced by the density variation, and reflected by the turbulence statistics, only very weak effects remain at the smallest scales of the flow (in terms of two point

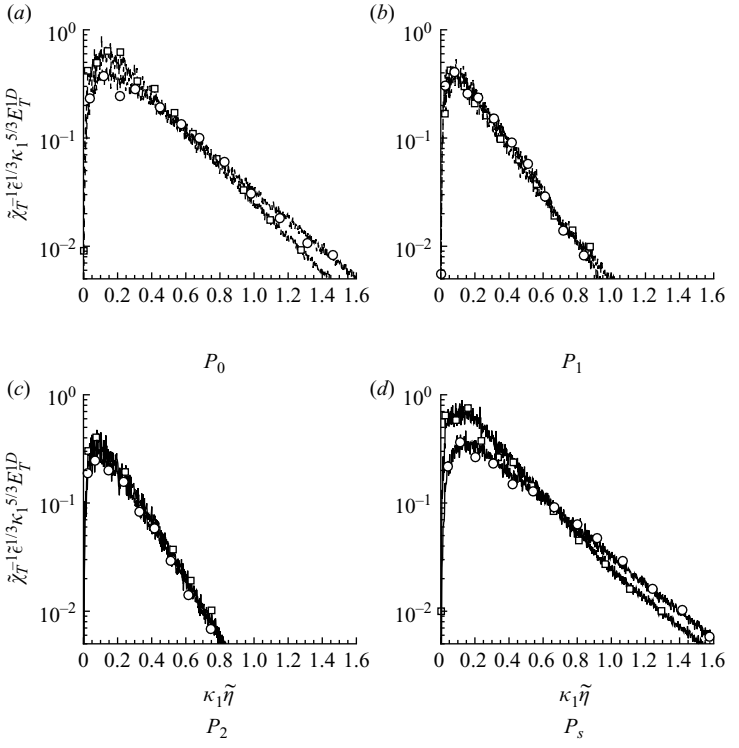

FIGURE 28. Reconstructed temperature spectra (○) from the mixture fraction spectra against the temperature spectra (□) at the four planes for Case D.

statistics). This is observed to apply for both the turbulence energy spectra and the mixture fraction spectra but not for the temperature in the dissipation subrange. It appears that the peculiarities observed in the dissipation subrange of the temperature spectra are related to the mixture fraction spectra through the known nonlinear (state) relationship for non-premixed two-stream combustion systems. An analogy with high-Schmidt-number mixing theories and a mathematical analysis are used to explore the relationship between the spectra of the mixture fraction, its moments and its one-point p.d.f. to the temperature spectrum. A rescaling of the temperature spectra using an overall rate of dissipation of temperature fluctuations and a temperature dissipation length scale is able to collapse the spectra in the dissipation subrange for all but one of the simulations. The second, more general technique allows a reconstruction of the temperature spectra from the mixture fraction spectra and shows that all cases are in relatively good agreement with the theory. The reconstruction reveals that the behaviour of the temperature spectrum reflects only the nonlinear nature of the relationship between mixture fraction and temperature. Moreover, different exponential decay rates in the dissipation subrange at different locations across the shear layer are attributed to different phase interactions of the mixture fraction moment spectra.

These results have implications for modelling of turbulent reacting flows where concepts extrapolated from constant-density incompressible flows appear to be relevant in describing some aspects of the statistics of reacting flows. The present results pertain only to non-premixed reacting flows and therefore shed no light on statistics of premixed reacting flows.

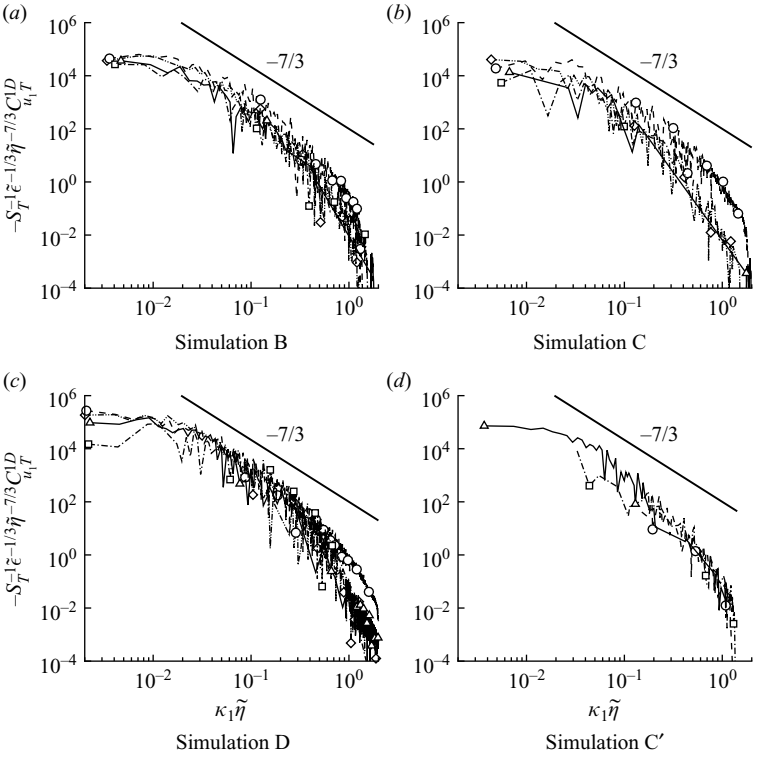

FIGURE 29. Temperature–velocity cospectra at different planes across the shear layer at the end of simulations for planes P_0 (○), P_1 (◇), P_2 (△) and P_s (□).

The authors thank the reviewers for many insightful and constructive comments. This work was supported in part by the ASC program of the Department of Energy (DOE) under subcontract no. B341492 of DOE contract no. W-7405-ENG-48 (while the second author resided at the California Institute of Technology) and by contract no. B523297 and the California Institute of Technology. Computational time was provided by the Los Alamos National Laboratory under the ASC program.

REFERENCES

ANTONIA, R. & MI, J. 1993 Temperature dissipation in a turbulent round jet. *J. Fluid Mech.* **250**, 531–551.

BARLOW, R. & KARPETIS, A. 2004 Measurements of scalar variance, scalar dissipation, and length scales in turbulent piloted methane/air jet flames. *Flow Turbul. Combust.* **72** (2), 427–448.

BATCHELOR, G. & TOWNSEND, A. 1949 The nature of turbulent motion at large wavenumbers. *Proc. R. Soc. Lond.* A **199** (1057), 238–255.

BILGER, R. 1980 Turbulent flows with nonpremixed reactants. In *Turbulent Reacting Flows* (ed. P. Libby & F. Williams), ch. 3, pp. 65–113. Springer.

BILGER, R. 1988 The structure of turbulent nonpremixed flames. *Proc. Combust. Inst.* **22**, 475–488.

BILGER, R. 2004 Some aspects of scalar dissipation. *Flow Turbul. Combust.* **72** (2), 93–114.

BILGER, R., SAETRAN, L. & KRISHNAMOORTHY, L. 1991 Reaction in a scalar mixing layer. *J. Fluid Mech.* **233**, 211–242.

BIRCH, A., BROWN, D., DODSON, M. & THOMAS, J. 1978 Turbulent concentration field of a methane jet. *J. Fluid Mech.* **88**, 431–449.

BOS, W., TOUIL, H. & BERTOGLIO, J.-P. 2005 Reynolds number dependency of the scalar flux spectrum in isotropic turbulence with a uniform scalar gradient. *Phys. Fluids* **17**, 125108.

Boyer, L. & Queiroz, M. 1991 Temperature dissipation measurements in a lifted turbulent-diffusion flame. *Combust. Sci. Tech.* **79** (1–3), 1–34.

Brown, G. & Roshko, A. 1974 On density effects and large structure in turbulent mixing layers. *J. Fluid Mech.* **64**, 775–816.

de Bruyn Kops, S., Riley, J. & Kosály, G. 2001 Direct numerical simulation of reacting scalar mixing layers. *Phys. Fluids* **13** (5), 1450–1465.

Buch, K. & Dahm, W. 1998 Experimental study of the fine-scale structure of conserved scalar mixing in turbulent shear flows. Part 2. Sc = 1. *J. Fluid Mech.* **364**, 1–29.

Burke, S. & Schumann, T. 1928 Diffusion flames. *Proc. Combust. Inst.* **1**, 2–11.

Campbell, L. 1964 On a class of polynomials useful in probability calculations. *IEEE Trans. Inf. Theory* **10** (3), 255–256.

Carter, C., Donbar, J. & Driscoll, J. 1998 Simultaneous CH planar laser-induced fluorescence and particle imaging velocimetry in turbulent nonpremixed flames. *Appl. Phys.* B **66** (1), 129–132.

Chen, Y.-C. & Mansour, M. 1996 Measurements of the detailed flame strucutre in turbulent H_2-air jet diffusion flames with line-Raman/Rayleigh/LIPF-OH technique. *Proc. Combust. Inst.* **26**, 97–103.

Clemens, N. & Paul, P. 1995 Effects of heat release on the near field flow structure of hydrogen jet diffusion flames. *Combust. Flame* **102** (3), 271–284.

Corrsin, S. 1961 The reactant concentration spectrum in trubulent mixing with a first order reaction. *J. Fluid Mech.* **11**, 407–416.

Dahm, W. 2005 Effects of heat release on turbulent shear flows. Part 2. Turbulent mixing layers and the equivalence principle. *J. Fluid Mech.* **540**, 1–19.

Dibble, R., Masri, A. & Bilger, R. 1987 The spontaneous raman-scattering technique applied to nonpremixed flames of methane. *Combust. Flame* **67** (3), 189–206.

Dimotakis, P. 2005 Turbulent mixing. *Annu. Rev. Fluid Mech.* **37**, 329–56.

Donbar, J., Driscoll, J. & Carter, C. 1998 Simultaneous CH planar laser-induced fluorescence and particle imaging velocimetry in turbulent flames. In *Thirty-Sixth Aerospace Sciences Meeting and Exhibit*, *AIAA* 98-0151. Reno, NV.

Donbar, J., Driscoll, J. & Carter, C. 1999 Strain rates measured along the wrinkled flame contour within turbulent nonpremixed jet flames. In *Joint Meeting of U.S. Section of the Combustion Institute*. Washington, DC.

Donzis, D., Sreenivasan, K. & Yeung, P. 2005 Scalar dissipation rate and dissipative anomaly in isotropic turbulence. *J. Fluid Mech.* **532**, 199–216.

Dowling, D. 1991 The estimated scalar dissipation rate in gas-phase turbulent jets. *Phys. Fluids* A **3** (9), 2229–2246.

Dowling, D. & Dimotakis, P. 1990 Similarity of the concentration field of gas-phase turbulent jets. *J. Fluid Mech.* **218**, 109–141.

Everest, D., Driscoll, J., Dahm, W. & Feikema, D. 1995 Images of the two-dimensional field and temperature gradients to quantify mixing rates within a non-premixed turbulent jet flame. *Combust. Flame* **101** (1), 58–68.

Fielding, J., Schaffer, A. & Long, M. 1998 Three-scalar imaging in turbulent non-premixed flames of methane. *Proc. Combust. Inst.* **27**, 1007–1014.

Frank, J. & Kaiser, S. 2008 High-resolution imaging of dissipative structures in a turbulent jet flame with laser Rayleigh scattering. *Exp. Fluids* **44**, 221233.

Gladnick, P., LaRue, J. & Samuelsen, G. 1990 Anisotropy in the near-field of a turbulent diffusion flame. In *Heat Transfer in Combustion Systems* (ed. B. Farouk, W. Grosshandler, D. Lilley & C. Presser), vol. 142, pp. 33–40. ASME.

Han, D. & Mungal, M. 2000 Simultaneous measurement of velocity and CH layer distribution in turbulent non-premixed flames. *Proc. Combust. Inst.* **28**, 261–267.

Han, D. & Mungal, M. 2003 Simultaneous measurement of velocity and CH distributions. Part 1: jet flames in co-flow. *Combust. Flame* **132** (3), 565–590.

Hermanson, J. & Dimotakis, P. 1989 Effects of heat release in a turbulent, reacting shear layer. *J. Fluid Mech.* **199**, 333–375.

Kaiser, S. & Frank, J. 2007 Imaging of dissipative structures in the near field of a turbulent non-premixed jet flame. *Proc. Combust. Inst.* **31**, 1515–1523.

Karpetis, A. & Barlow, R. 2002 Measurements of scalar dissipation in a turbulent piloted methane/air jet flame. *Proc. Combust. Inst.* **29**, 1929–1936.

Kida, S. & Goto, S. 1997 A Lagrangian direct-interaction approximation for homogeneous isotropic turbulence. *J. Fluid Mech.* **345**, 307–345.

Kolmogorov, A. 1941*a* Dissipation of energy in locally isotropic turbulence. *Dokl. Akad. Nauk SSSR* **32**, 19–21.

Kolmogorov, A. 1941*b* The local structure of turbulence in incompressible viscous fluid for very large reynolds numbers. *Dokl. Akad. Nauk SSSR* **30**, 299–303.

Kolmogorov, A. 1961 A refinement of previous hypotheses concerning the local structure of turbulence in a viscous incompressible fluid at high Reynolds number. *J. Fluid Mech.* **13**, 82–85.

Kosály, G. 1993 Frequency-spectra of reactant fluctuations in turbulent flows. *J. Fluid Mech.* **246**, 489–502.

Kounalakis, M., Sivathanu, Y. & Faeth, G. 1991 Infrared radiation statistics of nonluminous turbulent-diffusion flames. *J. Heat Transfer-Trans. ASME* **113** (2), 437–445.

Kraichnan, R. 1959 The structure of isotropic turbulence at very high reynolds numbers. *J. Fluid Mech.* **5**, 497–543.

Lide, D. (ed.) 1999 *Handbook of Chemistry and Physics*. CRC Press.

Liñán, A. 1974 Asymptotic structure of counterflow diffusion flames for large activation-energies. *Acta Astron.* **1** (7–8), 1007–1039.

Lumley, J. 1967 Similarity and the turbulent energy spectrum. *Phys. Fluids* **10**, 855–858.

Mahle, I., Foysi, H., Sarkar, S. & Friedrich, R. 2007 On the turbulence structure in inert and reacting compressible mixing layers. *J. Fluid Mech.* **593**, 171–180.

Markides, C. & Mastorakos, E. 2006 Measurements of scalar dissipation in a turbulent plume with planar laser-induced fluorescence of acetone. *Chem. Engng Sci.* **61** (9), 2835–2842.

Masri, A., Dibble, R. & Barlow, R. 1996 The structure of turbulent nonpremixed flames revealed by Raman–Rayleigh-LIF measurements. *Prog. Energy Combust. Sci.* **22** (4), 307–362.

McMurtry, P., Jou, W., Riley, J. & Metcalfe, R. 1986 Direct numerical simulations of a reacting mixing layer with chemical heat release. *AIAA J.* **24** (6), 962–70.

Meier, W., Barlow, R., Chen, Y.-L. & Chen, J.-Y. 2000 Raman/Rayleigh/LIF measurements in a turbulent $CH_4/H_2/N_2$ jet diffusion flame: experimental techniques and turbulence-chemistry interaction. *Combust. Flame* **123** (3), 326–343.

Monin, A. & Yaglom, A. 1971 *Statistical Fluid Mechanics*, vol. 1. MIT Press.

Muñiz, L. & Mungal, M. 2001 Effects of heat release and buoyancy on flow structure and entrainment in turbulent nonpremixed flames. *Combust. Flame* **126** (1–2), 1402–20.

Mydlarski, L. 2003 Mixed velocity-passive scalar statistics in high-reynolds-number turbulence. *J. Fluid Mech.* **475**, 173–203.

Mydlarski, L. & Warhaft, Z. 1998 Passive scalar statistics in high-péclet-number grid turbulence. *J. Fluid Mech.* **358**, 135–175.

Nagel, Z. & Dahm, W. 2007 Inner-scale effects of heat release in reacting turbulent shear flows. In *60th Annual Meeting of the Division of Fluid Dynamics*. APS, Salt Lake City, UT.

Namazian, M., Schefer, R. & Kelly, J. 1988 Scalar dissipation measurements in the developing region of a jet. *Combust. Flame* **74** (2), 147–160.

Nandula, S., Brown, T. & Pitz, R. 1994 Measurements of scalar dissipation in the reaction zones of turbulent nonpremixed H_2 air flames. *Combust. Flame* **99** (3–4), 775–783.

Noda, S., Mori, H., Hongo, Y. & Nishioka, M. 2005 Nonpremixed flamelet statistics at flame base of lifted turbulent jet nonpremixed flames. *JSME Int. J. Ser.ies* B **48** (1), 75–82.

O'Gorman, P. & Pullin, D. 2003 The velocity-scalar cross spectrum of stretched spiral vortices. *Phys. Fluids* **15** (2), 280–291.

Overholt, M. & Pope, S. 1996 Direct numerical simulation of a passive scalar with imposed mean gradient in isotropic turbulence. *Phys. Fluids* **8** (11), 3128–48.

Pantano, C., Sarkar, S. & Williams, F. 2003 Mixing of a conserved scalar in a turbulent reacting shear layer. *J. Fluid Mech.* **481**, 291–328.

Peters, N. 1984 Laminar diffusion flamelet models in non-premixed turbulent combustion. *Prog. Energy Combust. Sci.* **10** (3), 319–339.

Pickett, L. & Chandhi, J. 2003 Structure of a reacting hydrocarbon-air planar mixing layer. *Combust. Flame* **132** (1), 138–156.

Pope, S. 1985 PDF methods for turbulent reactive flows. *Prog. Energy Combust. Sci.* **11**, 119–192.

Pope, S. 2000 *Turbulent Flow*. Cambridge University Press.

Rehm, J. & Clemens, N. 1998 The relationship between vorticity/strain and reaction zone structure in turbulent non-premixed jet flames. *Proc. Combust. Inst.* **27**, 1113–1120.

Renfro, M., Gore, J., King, G. & Laurendeau, N. 2000 Self-similarity of hydroxyl-concentration temporal statistics in turbulent nonpremixed jet flames. *AIAA J.* **38** (7), 1230–1236.

Richardson, L. 1922 *Weather Prediction by Numerical Process*. Cambridge University Press.

Sabini, G., Shieh, G. & Givi, P. 1996 Modeling of the fluctuations and the frequency-spectra of reactants in turbulent scalar mixing layers. *Chem. Engng Commun.* **154**, 147–181.

Saddoughi, S. & Veeravalli, S. 1994 Local isotropy in turbulent boundary layers at high reynolds numbers. *J. Fluid Mech.* **268**, 333–372.

Schumacher, J., Sreenivasan, K. & Yeung, P. 2005 Very fine structures in scalar mixing. *J. Fluid Mech.* **531**, 113–122.

Seitzman, J., Ungut, A., Paul, P. & Hanson, R. 1990 Imaging and characterization of OH structures in a turbulent nonpremixed flame. *Proc. Combust. Inst.* **23**, 637–644.

Seshadri, K. & Peters, N. 1988 Asymptotic structure and extinction of methane–air diffusion flames. *Comusti. Flame* **73**, 23–44.

Shutterly, H. 1963 General results in the mathematical theory of random signals and noise in nonlinear devices. *IEEE Trans. Inf. Theory* **9** (2), 74–84.

Sreenivasan, K. 2004 Possible effects of small-scale intermittency in turbulnt reacting flows. *Flow Turbul. Combust.* **72** (2), 115–131.

Su, L. & Clemens, N. 2003 The structure of fine-scale scalar mixing in gas-phase planar turbulent jets. *J. Fluid Mech.* **488**, 1–29.

Tacina, K. & Dahm, W. 2000 Effects of heat release on turbulent shear flows. Part 1. A general equivalent principle for non-buoyant flows and its application to turbulent jet flames. *J. Fluid Mech.* **415**, 23–44.

Tennekes, H. & Lumley, J. 1972 *A First Course in Turbulence*. MIT Press.

Theron, M. & Bellenoue, M. 2006 Experimental investigation of the effects of heat release on mixing processes and flow structure in a high-speed subsonic turbulent h_2 jet. *Combust. Flame* **145** (4), 688–702.

Thompson, W. 1954 The response of a non-linear system to random noise. *Proc. IEEE* **102**, 46–48.

Tsurikov, M. & Clemens, N. 2002 The structure of dissipative scales in axisymmetric turbulent gas-phase jets. In *40th Aerospace Sciences Meeting and Exhibit*, vol. 164. Reno, NV.

Uberoi, M. & Freymuth, P. 1969 Spectra of turbulence in wakes behind circular cylinders. *Phys. Fluids* **12** (7), 1359–1363.

Vedula, P., Yeung, P. & Fox, R. 2001 Dynamics of scalar dissipation in isotropic turbulence: a numerical and modelling study. *J. Fluid Mech.* **433**, 29–60.

Vervisch, L. & Poinsot, T. 1998 Direct numerical simulation of non-premixed turbulent flames. *Annu. Rev. Fluid Mech.* **30**, 655–91.

Wallace, A. 1981 Experimental investigation of the effects of chemical heat release in the reacting turbulent plane shear layer. PhD thesis, The University of Adelaide (also AFOSR Rep. TR-84-0650).

Wang, G. & Barlow, R. 2008 Spatial resolution effects on the measurement of scalar variance and scalar gradient in turbulent nonpremixed jet flames. *Exp. Fluids* **44**, 633645.

Wang, G., Clemens, N. & Varghese, P. 2005 High-repetition rate measurements of temperature and thermal dissipation in a non-premixed turbulent jet flame. *Proc. Combust. Inst.* **30**, 691–699.

Wang, G.-H., Clemens, N., Varghese, P. & Barlow, R. 2008 Turbulent time scales in a nonpremixed turbulent jet flame by using high-repetition rate thermometry. *Comust. Flame* **152**, 317–335.

Wang, G., Karpetis, A. & Barlow, R. 2007 Dissipation length scales in turbulent nonpremixed jet flames. *Combust. Flame* **148** (1), 62–75.

Warhaft, Z. 2000 Passive scalars in trubulent flows. *Annu. Rev. Fluid Mech.* **32**, 203–240.

Williams, F. A. 1985 *Combustion Theory*. Benjamin/Cummings.

Wygnanski, I. & Fielder, H. 1969 Some measurements in self-preserving jet. *J. Fluid Mech.* **38**, 577–612.

Zhang, H., Wang, D. & Tong, C. 2004 On conditional scalar increment and joint velocity-scalar increment statistics. *New J. Phys.* **6** (38).